Journal of Geophysical Research: Oceans
DOI 10.1002/2018JC013887

Fronts of the Malvinas Current System: surface and subsurface expressions revealed by satellite altimetry, Argo floats, and Mercator operational model outputs

Camila Artana[1], Jean-Michel Lellouche[2], Young-Hyang Park[1], Gilles Garric[2], Zoé Koenig[1], Nathalie Sennéchael[1], Ramiro Ferrari[3], Alberto R. Piola[4], Martin Saraceno[5] and Christine Provost[1].

[1]: Laboratoire LOCEAN-IPSL, Sorbonne Université (UPMC, Univ. Paris 6)-CNRS-IRD-MNHN, Paris, France

[2]: MERCATOR-OCEAN, Parc Technologique du Canal, Ramonville St. Agne, France,

[3]: CIMA/CONICET-UBA and UMI IFAECI-3351, Buenos Aires, Argentina

[4]: Departamento de Oceanografía, Servicio de Hidrografía Naval, DCAO/FCEN/UBA and UMI IFAECI-3351, CONICET, Buenos Aires, Argentina

[5]: CIMA/CONICET-UBA, DCAO/FCEN/UBA and UMI IFAECI-3351, Buenos Aires, Argentina

This article has been accepted for publication and undergone full peer review but has not been through the copyediting, typesetting, pagination and proofreading process which may lead to differences between this version and the Version of Record. Please cite this article as doi: 10.1029/2018JC013887

Received: Feb 07, 2018; Revised: May 03, 2018; Accepted: May 07, 2018

Key points:

- Good agreement between Mercator operational model outputs and mooring data near the complex region of the Brazil-Malvinas Confluence.
- Thresholds in potential density at mid-depths (340-600 m) match dynamic topography markers of the mean position of fronts in the southwest Atlantic
- Potential density at mid-depths documents eddies detached from the Polar Front feeding the Malvinas Current.

Abstract:

We examine the surface and subsurface signature of ocean fronts closely associated with the Malvinas Current dynamics. We first evaluate the performances of the Mercator-ocean eddy permitting (1/12° spatial resolution) global operational system in the Southwestern Atlantic Ocean over the last 10 years (2007-2016) using satellite, Argo float and in situ data collected near 41°S. Observations versus model comparisons show that the model correctly reproduces the general circulation and the complex hydrographic features of the study area including the vicinity of the Brazil-Malvinas Confluence. The model outputs accurately match the observations except in June 2015. The causes for the June 2015 mismatch are analyzed. We then used the model and satellite altimetry to identify isolines of absolute dynamic topography (ADT) and potential density at different depths associated with the mean front location and establish their correspondence with specific water mass boundaries. Frontal displacements as depicted in satellite ADT, model ADT and model potential density at 450 m are in general agreement. The ADT and potential density at 450 m provide non-identical and complementary information on eddies shed by the Polar Front (PF): while ADT depicts the surface circulation with PF eddies entrained into the energetic circulation over the deep Argentine Basin, potential density at 450 m is more effective at monitoring PF eddies feeding the Malvinas Current.

1. Introduction

The Malvinas Current (MC) is the northward flowing western boundary current of the Southwestern Atlantic Ocean (Figure 1a). The MC originates from the northern Drake Passage as an offshoot of the Antarctic Circumpolar Current (ACC). The ACC, in the Drake Passage, is organized in three main fronts, which correspond to water mass boundaries as well as deep-reaching jets of eastward flow: the Subantarctic Front (SAF), the Polar Front (PF), and the Southern ACC Front (SACCF) (Nowlin et al., 1977; Orsi et al., 1995). The complex bottom topography downstream of Drake Passage strongly constrains the ACC flow (Artana et al., 2016). The SAF makes a sharp northward turn, proceeds through the narrow East of Burdwood Bank passage, and enters the Argentine Basin crossing the Malvinas Plateau (Figure 1a). The northward extension of the SAF is referred to as the MC. The MC follows the steep Patagonian continental slope up to 38°S where it encounters the Brazil Current which is limited by the Brazil Current Front (BCF) (Roden, 1986). After the collision, both currents veer offshore and separate from the slope. The MC performs a sharp cyclonic loop towards the South and it is then called Malvinas Return Current. The Brazil Current overshoots anticyclonically reaching latitude of 44°S (Figure 1a). The eddy kinetic energy (EKE) in the Brazil-Malvinas Confluence (BMC) region is amongst the largest of the world ocean (>2000 cm^2s^{-2}) (Figure 1b). In contrast, the eddy kinetic energy over the MC is low (<100 cm^2s^{-2}). The topographic barriers of the North Scotia Ridge and the Malvinas Plateau between the Drake Passage and the Argentine Basin restrict the northward penetration of mesoscale eddy activity north of 53°S (Artana et al., 2016) (Figure 1b).

In situ data in the MC are rather scarce. Direct current observations in the north of the MC (41°S) showed that the MC has an equivalent barotropic structure due to the weak stratification and the steep topography (Vivier and Provost, 1999). High-resolution hydrographic and current data

indicated that at 45°S the MC flow is concentrated in two narrow jets located over two terraces (centered at 200 and 1400 m) in the continental slope (Piola et al., 2013). The two jets merge further downstream at ~41°S. Recent studies of the MC dynamics using altimetry and Argo floats suggested that at times, the MC is cut from its source downstream of Drake Passage by anticyclonic anomalies propagating westward along the Malvinas Escarpment at 48°S (Artana et al., 2016). However, these blocking events at 48°S do not seem to affect the MC flow at 41°S, as a cyclonic recirculation cell is established between 38°S and 48°S, with the MC being its western boundary. Extreme transport maxima at 41°S (reaching 50 Sv) appear to be related with cyclonic eddies detached from the PF (48°W-48°S), which propagate northward above the 4000 m isobath up to the BMC (Artana et al., 2018).

A new data set was gathered in the MC near its encounter with the Brazil Current from year-long moorings including ADCP (Acoustic Doppler Current Profiler) velocity profiles and temperature and salinity time series as part of the CASSIS-Malvinas project (Saraceno et al., 2017; Figure 1e). A precise comparison between velocities derived from satellite altimetry and 20-day low-pass filtered velocities from current meters deployed at ~300 m depth showed high correlations (larger than 0.8, Ferrari et al., 2017). In the 24 year-long altimetry record, two modes dominate sea level anomaly variations in the southwestern portion (west of 52°W) of the BMC region: the first mode is associated with a latitudinal migration of the SAF, and the second with a longitudinal displacement of the Brazil Current overshoot (Ferrari et al., 2017). The BMC location in numerical simulations is highly sensitive to the bottom friction representation and to the spatial distribution of the ACC volume transport through Drake Passage as well as to the vertical and horizontal resolutions of the model (Combes and Matano, 2014). Consequently, numerical studies of the region have been hampered by the difficulty to simulate the proper location of the BMC. Ocean

operational models that assimilate satellite altimetry (e.g. Lellouche et al., 2013) are a priori more likely to have the BMC at the correct location. The new data set from the CASSIS-Malvinas project provides a unique opportunity to examine in detail how an operational model behaves in this complex region.

The main objective of this work is to examine the signature of the fronts of the Malvinas Current System as revealed by the spatial and temporal patterns of satellite altimetry and model density fields. The ACC fronts are associated with large horizontal gradients both in potential density at 400 m and in absolute dynamic topography (Provost et al., 2011). The large horizontal gradients can be associated with specific isopycnals in potential density at 400 m and in absolute dynamic topography. Artana et al., (2016) defined criteria in potential density and dynamic topography for the three main ACC fronts (SAF, PF and SACCF) and showed that in Drake Passage the location of these fronts inferred from potential density at 400 m determined from Argo float data is in good agreement with the front location inferred from mean absolute dynamic topography. The three ACC fronts are composed of branches with distinct dynamic topography signatures (Sokolov and Rintoul, 2009a, 2009b; Barré et al., 2011). In Drake Passage, those branches are from north to south: two branches for the SAF: SAF-N (north) and SAF-M (main); three branches for the PF: PF-N (north), PF-M (main) and PF-S (south); and two branches for the SACCF: SACCF-N (north) and SACCF-S (south) (Figure 1). Here we examine the signature of the fronts closely associated with the MC dynamics along the western slope of the Argentine Basin, or MC system, namely the SAF-M, the PF-M, the PF-N and the BCF. For this purpose we use data from Argo floats and from satellite altimetry, as well as outputs from the current global Mercator Ocean high resolution (1/12°) operational model PSY4V3R1 (hereafter PSY4). A prerequisite to carry out the present analysis is to first assess the performance of PSY4 in the southwestern Atlantic with a focus on

the MC. In particular, we compare the daily model outputs with the recent mooring data (December 2014 - November 2015) to evaluate the model performance in the region of the BMC.

The paper is structured as follows: the Mercator Ocean global model, *in situ* and satellite data are described in section 2. In section 3 we compare model outputs to altimetry and Argo floats to assess the model skill in reproducing the circulation and hydrography in the study area over the 10-year period of model outputs (2007-2016). The daily model outputs are also confronted with *in situ* time series near the BMC. In section 4, we examine the potential density and sea surface height characteristics of the fronts of the MC system. Similarities and differences in the dynamic height and density variations are discussed. Finally, section 5 summarizes and concludes.

2. Model outputs and data

2.1 Mercator Ocean operational model

Since October 19, 2016, and in the framework of Copernicus Marine Environment Monitoring Service (CMEMS, http://marine.copernicus.eu/), Mercator Ocean delivers in real-time daily services (weekly analyses and daily 10-day forecasts) with a new global 1/12° high resolution ocean model system (Lellouche et al., 2018). The vertical discretization comprises 50 levels with 22 levels in the upper 100 m. As a result, vertical resolution is 1 m near the surface and decreases to 450 m resolution near the bottom. The physical model component is the NEMO (Nucleus for European Modelling of the Ocean) platform (Madec et al., 2008) driven at the surface by the Integrated Forecast System ECMWF (European Centre for Medium-Range Weather Forecasts) atmospheric analyses and forecasts. Observations are assimilated by means of a reduced-order Kalman filter with a 3D multivariate modal decomposition of the forecast error and a 7-day

assimilation cycle. Along-track altimeter data (Pujol et al., 2016), satellite Sea Surface Temperature and Sea-Ice Concentration from OSTIA (Donlon et al., 2012) and *in situ* temperature and salinity vertical profiles from the CORA 4.2 in situ database (Cabanes et al., 2013; Szekely et al., 2016) are jointly assimilated. Moreover, a 3D-VAR scheme provides a correction for the slowly-evolving large-scale biases in temperature and salinity. This Mercator Ocean global ocean system PSY4 provides daily outputs of temperature, salinity, currents, sea-ice and sea level (http://marine.copernicus.eu/) for the 2007-2016 period.

2.2 *In situ* data

We used the Argo float data (http://www.usgodae.org) to assess how the Mercator model outputs represent the thermohaline structure of the southwestern Atlantic Ocean. Argo floats provide temperature and salinity profiles between 0 and 2000 db every 10 days. The typical vertical resolution of the Argo observations is ~10 dbar for the 0-150 m layer, ~50 dbar for the 150-300 m layer, 75 dbar for the 300-500m layer and 100 dbar for the depths below 500 m. We apply the automatic Quality Control (QC) filter from the Argo data center (Argo Data Management, 2013) to all the Argo float profiles. Despite this QC, we detected profiles from long-lived Argo floats (>5 years) in the center of the Argentine Basin (platform numbers 3900266, 3900439, 3900569 and 3900797) with a significant salinity offset probably due to biofouling (Jia et al., 2016). Consequently, 725 Argo profiles presenting large salinity biases are not used in the comparison. We were conservative and removed the corresponding temperature profiles too. As a result, 21397 profiles from 414 floats drifting in the southwestern Atlantic Ocean over the period 2007-2016 are included in this assessment. There are between 1400 and 2000 profiles each year, except in 2015 and 2016 during which years the number of profiles doubles (3200 in 2015, 4000 in 2016). The spatial distribution of profiles is quite homogeneous. Model outputs are collocated and compared

to these profiles. The Argo float profiles are not independent data since they are included in the assimilation procedure via the CORA 4.2 data base. However, the integrated nature of operational system, combining satellites and in situ observations with the model dynamics, does not guarantee that all information is retained.

The model outputs are also compared with the independent *in situ* time series of temperature, salinity and velocity from three moorings deployed between December 2014 and November 2015 (Saraceno et al., 2017). The moorings were lined up on the western slope of the Argentine Basin close to the BMC at 41°S along Jason satellite track #26 (moorings A1, M1 and M2, in red in Figure 1e). The array consisted of a bottom mooring (A1) equipped with an ADCP and a Conductivity-Temperature (CT) sensor, installed at 1000 m depth, and two tall-moorings: M1 at 1300 m depth comprising 3 current-meters and 3 temperature and conductivity sensors (CT), and M2 at 1500 m depth, equipped with 4 current-meters and 4 CT sensors. For the purpose of comparison, the model outputs have been collocated in space and time to the *in situ* data. *In-situ* and model velocities are rotated (+37.98 degrees) to decompose into the along and across-slope components, i.e. parallel and perpendicular to the local bottom slope. *In situ* current-meter data have been 10-day low-pass filtered. Indeed, a preliminary comparison between model velocities and *in situ* velocities filtered with different cut-off periods (2, 5, 10, and 20 days) indicates that a 10-day cut-off period provides a satisfactory agreement. In addition, the *in situ* salinity and temperature data have been low-pass filtered with a Loess filter with a cutoff period of 2 days to remove tidal and inertial variability.

2.3 Satellite data

In order to assess the satellite data assimilation performance, model outputs of Sea Surface Temperature (SST) and sea surface height are compared to satellite data. Satellite SST fields used

are from the Operational Sea Surface Temperature and Sea Ice Analysis (OSTIA) system (~25 km of resolution, http://marine.copernicus.eu/). Two different types of satellite altimetric products are used: DUACS delayed time altimeter gridded products and along-track satellite altimetric data (Pujol et al, 2016). Both are produced as part of the CMEMS. The gridded product includes data from all available altimeters at any given time. This product comprises maps of sea level anomaly (SLA), absolute dynamic topography (ADT), surface geostrophic velocities and surface geostrophic velocity anomalies with a spatial resolution of 1/4º on a Mercator regular grid and a daily sampling. The along-track product consists of ADT and SLA from available satellites with a temporal sampling ranging between 10 and 35 days depending on the satellite and an along-track sampling of 14 km. The observed ADT product is the sum of the observed SLA and the Mean Dynamic Topography (MDT) CNES-CLS13 (Rio et al., 2014). Since the latter is different from the MDT used by Mercator system PSY4, and in order to be able to compare the ADT from both products, we correct the MDT used by PSY4 applying an offset-computed over the period 2007-2016. The offset was computed as the mean difference between the mean observed ADT over 2007-2016 and the mean model ADT over the same period and it is of 45 cm.

3. Performance of the Mercator Model

3.1 Comparison to satellite altimetry surface circulation (2007-2016)

The large-scale circulation patterns are well represented in the model outputs (Figure 1 a and c). Satellite data and model outputs show a similar location of the BMC, SAF and BCF. In general, the model surface velocities are slightly larger (by a few cm/s) than the satellite-derived surface-geostrophic velocities. This may be due to the better spatial resolution of the model (1/12 degree

versus 1/4 degree for altimetry). In the MC core over the 1000-1500 m isobath, between 47°S and 38°S, the model mean surface velocities reach 65 cm/s, that is ~ 12 cm/s larger than the mean satellite-derived surface geostrophic velocities. The model mean surface velocities at 45°S show the presence of the two relatively narrow jets in the MC (following the 200 and 1400 m isobaths), in agreement with results from Piola et al. (2013). The mean position of each jet also coincides with the mean position of the two branches of the SAF: the SAF-M and the SAF-N. The mean locations of the other ACC fronts, the three branches of the PF and the two SACCF branches, are also well reproduced in the model.

The model EKE shows the same spatial patterns as the satellite-deduced EKE (Figures 1b, d) which is not surprising since the model assimilates the along-track satellite data. In general, the model EKE is larger than the satellite-derived EKE over the Argentine Basin by about 20%. The model grid resolves mesoscale features that are aliased in the altimetric grid (1/4°).

3.2 Comparison to hydrography from Argo float data (2007-2016)

The ACC fronts are characterized by strong horizontal density gradients at about 400 m depth (Provost et al., 2011). Consequently, potential density at 400 m depth can be used to infer the location of the ACC fronts (Artana et al., 2016). Several model depths (380, 450 and 540 m) below the reach of seasonal temperature variations were examined (section 4.1). As an example, in the following, we compare model outputs at 450 m to observations from Argo floats.

Maps of salinity, potential temperature, and potential density at 450 m from Argo floats and the model means are shown in Figure 2. The large-scale hydrographic patterns at 450 m are well represented in the model. Relatively large potential density (>27.1 kg/m^3) associated with fresh (< 34.2 psu) and cold (< 3.5°C) subantarctic waters are observed in the southern Argentine Basin

and in the MC. Potential density values less than 26.9 kg/m^3 are associated with salty (> 34.5 psu) and warm (>5°C) subtropical waters located north of ~ 40 ºS. The center of the Argentine Basin appears as a region of intermediate potential density values (between 27.00 and 27.10 kg/m^3). In order to achieve a more precise comparison, model outputs of temperature, salinity and potential density are collocated in time and space at each Argo float profile. The differences between the collocated model outputs and the Argo observations do not exhibit any significant bias. Individual differences greater than ± 1.0°C in temperature, ± 0.2 psu in salinity and ± 0.2 kg/m^3 in potential density are found in the southern edge of the subtropical gyre which is populated with energetic mesoscale structures. In contrast, differences in Subantarctic Waters are negligible (not shown).

To further illustrate the model skills in the MC we compare model outputs with data from two particular Argo floats (Figure 3). These floats provided profiles every day and were present in the database assimilated by PSY4. Moreover, none of these profiles were rejected by the additional QCs implemented in PSY4. The first Argo float (platform number 6901650, hereafter float 1), data described in Artana et al. (2016), was trapped in a cyclonic eddy shed by the PF which broke apart and dissipated over the Malvinas Plateau. The second Argo float (platform number 6901654, hereafter float 2) drifted from 53°S to 36°S over the upper Argentinean continental slope during a year (from May 2015 to May 2016). From 24 June to 29 July 2015, float 1 was inside a cyclonic eddy and recorded a temperature minimum of 0.8°C at 200 m corresponding to the Winter Water coming from the south of the PF (Figures 3a, b). Winter Water is well reproduced in the time-space collocated model outputs (Figure 3c). In early August, the eddy disintegrated and the float and the model outputs show relatively warm (3.5 to 4.5°C) temperatures extending over the upper 600 m of the water column (Figures 3b, c). Float 2 followed the upper continental slope over depths varying between 300 and 1500m from May 2015 to May 2016 (Figure 3d). Daily Argo float

profiles of the upper 1000 m of the water column show a wide range of salinity values from 33.68 to 34.81 (Figure 3e). The salinity below 300 m is ~34.1 psu in both the Argo profiles and in the model (Figures 3e, f). The model reproduces the major salinity variations in the upper water column, with a low salinity (<34.0 psu) derived from the continental shelf when the float drifted over depths shallower than 500 m (from 53 to 49°S and from 40 to 37.5°S).

3.3. Validation near the BMC: comparison to mooring data at 41° S

Daily model outputs of velocities, temperature, salinity and density are compared to *in situ* mooring time series gathered near the BMC from December 2014 to November 2015 (Figure 1e).

3.3.1 Comparison of means and standard deviation

Model and in situ means of temperature, salinity and potential density are shown in Figures 4a, b, c and Table 1. Model mean temperature (salinity) and *in situ* mean temperature (salinity) do not differ more than 0.2°C (0.05 psu) and differences in mean potential density do not exceed 0.07 kg/m^3. The water mass composition derived from model outputs is in good agreement with the present knowledge of water masses at 41°S (e.g. Maamaatuaiahutapu et al., 1994; Table 2). The mean temperature and salinity of the upper 100 m (>4.8°C, ~34.05 psu) correspond to the light Subantarctic Surface Water (SASW) (σ_θ <27.00 kg/m^3). Low salinity water in the western part of the section (<34 psu) corresponds to a mixture of SASW with slope water. The low salinity (<34.3 psu) layers below correspond to Antarctic Intermediate Waters (AAIW). Three varieties of AAIW can be distinguished in the region (Provost et al., 1995): a light upper AAIW (AAIW-U) (27.00 < σ_θ < 27.14 kg/m^3), a central AAIW (AAIW-C) (27.14 < σ_θ < 27.29 kg/m^3) and a lower AAIW (AAIW-L) (27.29 < σ_θ < 25.35 kg/m^3). The AAIW-U and the AAIW-C are classified as

Subantarctic Mode Waters in Provost et al. (1995). Subantarctic Mode Waters are precursors of the lighter varieties of Antarctic Intermediate Water (McCartney, 1977; Piola and Gordon, 1989). Underneath the AAIW Upper Circumpolar Deep Water (UCDW) with temperatures lower than 3°C and salinity greater than 34.3 psu corresponds to potential density between 27.35 and 27.73 kg/m^3. Finally, CDW and Lower CDW (LCDW) (2.3<T< 2°C, S >34.75 psu, and 27.73< σ_θ < 27.80 kg/m^3; and T< 2°C, S >34.75 psu, and σ_θ >27.80 kg/m^3, respectively) are found between 2000 m and 3500 m.

In general, the standard deviations of model temperature, salinity and density present similar orders of magnitude (Figures 4d, e, f; Table 1). The *in situ* temperature standard deviation increases to about 0.6° C in the upper 500 m in the eastern part of the section and the model provides similar temperature standard deviation (~0.4° C). The *in situ* salinity and potential density standard deviations show a conspicuous maximum centered at 1000 m depth, also present in the model. These local standard deviation maxima in salinity and density present model (*in situ* data) values of 0.09 (0.08) psu and 0.08 (0.09) kg/m^3, respectively. The standard deviation maxima correspond to the densest varieties of AAIW and UCDW mean depth range. Close to the sea floor, the model standard deviations of temperature (0.2°C), salinity (0.07 psu) and potential density (0.05 kg/m^3), are slightly larger than the *in situ* data.

In situ and model means of the velocity components are shown in Figure 5 and Table 1. In the upper slope, at the ADCP location (A1) differences between the mean model velocities and the mean *in situ* velocities are less than 3.5 cm/s for the along-slope component and 4 cm/s for the across-slope component. The agreement between the model and the along-slope *in situ* mean velocities decreases towards the outer slope (Figure 5a). The model along-slope mean velocities

are larger than in the observations by about 8 cm/s and 12 cm/s at M1 and M2, respectively (Table 1). The model across-slope mean velocities agree with observations (differences less than 3 cm/s, Table 1) and present negative values in the upper slope (between km -20 and km 40) and positive values further offshore (between km 80 and km 140) leading to a divergence in the mean flow over the middle slope (Figure 5b).

The model and the observations show large standard deviation of the along-slope velocity component (> 20 cm/s) in the upper levels of ADCP (A1) (Figure 5c). The across-slope velocity component shows large standard deviation values (>15 cm/s) in the offshore part of the section (> 80 km) apparent in the model and the shallowest current meter at M2, associated with the mesoscale activity of the Brazil Current overshoot (Figure 5d). Differences between the standard deviation of the in situ and model velocity component over the slope are smaller than 3 cm/s and 2.5 cm/s, for the along and across-slope velocities respectively (Table 1). At the outer-slope, model velocity standard deviations are smaller than *in situ* standard deviations by about 6 cm/s for the along-slope component and 3 cm/s for the across-slope component.

3.3.2 Comparison of time series

The analysis of satellite altimetry and direct current observations collected from December 2014 to November 2015 showed that the MC at 41°S went through two distinct regimes based on the intensity of the along-slope flow at 41°S referred to as “weak Malvinas” (December 2014 and May to -September 2015) and “strong Malvinas” (early January to mid-April 2015 and mid-September to the end of November 2015) (Ferrari et al., 2017). The distinct regimes at 41°S can be identified in the i*n situ* ADCP velocity components (Figures 6a, c). During the strong regime, along-slope

velocities at 300 m reach values as large as 70 cm/s. During the weak regime, along-slope velocities at 300 m remain below 30 cm/s and, in some occasions, the ADCP recorded negative along-slope velocities (such as in late June 2015, Figure 6a). During the "strong Malvinas" regime at 41°S the across-slope component is mainly negative (reaching values as large as -24 cm/s at 300 m) while during "weak Malvinas" regime at 41°S is mainly positive (values larger than 16 cm/s in some occasions) (Figure 6c). The model reproduces the two regimes and the pattern of velocity variations at 41°S (Figures 6b, d). However, there is less agreement between the *in situ* and the model velocities during the "weak Malvinas" period. In particular, during June 2015 model along-slope velocities at 328 m depth reach a maximum of 53 cm/ while *in situ* velocities at that time are lower than 25 cm/s (Figures 6e, f). Comparisons of along and across slope model velocity time series at the outer upper-level moorings (M1 and M2, not shown) also show the departure of the model from the observations in June 2015.

In the following, we carefully compare model outputs to the assimilated satellite data at the BMC in June 2015 to seek an explanation for the discrepancies pointed out above.

3.3.3 Comparison to satellite data along a section at 41°S

The altimetric along-track SLA time series along a 160 km-long portion of ground track #26 (Figure 7a and Figure 1a) shows large positive anomalies (~30 cm) in the 50 - 160 km range during the "weak Malvinas" period. The large positive anomalies are associated with an anomalous southern position of the SAF (Ferrari et al., 2017). The model SLA time series interpolated at the location of ground track #26 also shows positive anomalies, but with much lower intensity (~20 cm) than the altimeter observations during the "weak Malvinas" period (Figure 7b). During the

"strong Malvinas" regime differences between interpolated model SLA and altimetric SLA are less than 5 cm (Figure 7c). Major differences (~10 cm) occur during the "weak Malvinas" regime in the offshore part of the section (50 - 160 km range). During June 2015, differences are particularly large (>25 cm) suggesting that the satellite SLA from this month might not be correctly assimilated in the model. The 10-year long time series of the differences between the model and satellite SLA (Figure 7d) clearly illustrate that the large values of June 2015 are unique and that differences are small before 2015.

Figures 8 a and b show the satellite and model ADT gridded maps on 10 June 2015 superimposed to the along track ADT satellite product available for the week centered at this date. As might be expected the agreement between the ADT gridded map and the along-track ADT product is excellent with differences away from the coast not exceeding 2 cm, which is within the altimetric error (Figure 8c). Both, the gridded altimetric ADT maps and the along track products, show the location of the SAF to the south of the mooring line (black section in Figure 8a). In contrast, the model ADT differs significantly from the altimetric along-track product, which is actually the product involved in the assimilation procedure (Figure 8b). Major differences (larger than 30 cm) are found over the offshore portion of the slope (40- 41°S, 54-56°W, Figure 8d). At this date, the model SAF is located further north of what it should be according to the along track altimetric product and the *in-situ* velocity observations.

In addition to along-track altimeter data the Mercator model PSY4 assimilates SST maps from OSTIA (section 2.3). In contrast to information provided by altimetric data, the SST map from OSTIA on 10 June 2015 indicates that the northernmost extension of the MC is located north of the mooring line (Figure 8e). The model SST map at this date (Figure 8f) is similar to the OSTIA SST, suggesting that, at this particular date, the information provided by the SST map prevails

over the altimetric observations in the data assimilation scheme. The cloud coverage on 10 June 2015 exceeded 70 % in the BMC region (not shown) precluding the precise observations of high-resolution SST. In general, the OSTIA maps in the BMC for June 2015 are uncertain. The mean percentage of cloud cover for the region over the 10 year-long period is 50% and its associated standard deviation is 30%. Thus, infrared SST observations are often lacking in this region. Consequently, this analysis suggests that the weight given to the SST observations within the assimilation scheme should be adjusted as a function of the cloud cover.

The performance of the model outputs close to the BMC is remarkably good except in June 2015 when the surface circulation is anomalous with an exceptional southern SAF position (Ferrari et al., 2017) and the assimilation scheme follows uncertain SST information due to cloud-covered region. This evaluation of the performance of Mercator operational model over the 10 years (2007-2016) showed that the model reproduces the assimilated Argo float profiles and dynamic topography quite faithfully in the study area. In the following section we use the model outputs to examine the signature of the major fronts of the MC system in ADT and potential density at depths.

4 Fronts of the MC system in ADT and potential density at 450m

4.1 Mean location of the fronts

The major fronts in the Malvinas Current System (SAF-M, PF-N and PF-M) correspond to large gradients in ADT (Figure 9a) and in potential density (σ_θ) away from near-surface seasonal temperature variations (Figures 9c, e). The location of the large horizontal mean gradients correspond to particular contours of mean ADT (Figure 9b, Table 3) and particular contours of mean potential density depending upon the depth considered (Figures 9 d, f and Table 3). The

mean positions of the MC system fronts based on maximum horizontal density gradients at 380, 450 and 540 m are in close agreement (Figures 10a, b and 9c, e). Then, in the following we analyse front locations based on maxima in the density gradient fields at 450 m (Figures 10a, b). For the SAF-M, the 0 cm ADT contour coincides with the ADT gradient maximum while two potential density values (27.15 and 27.10 kg/m^3) are used to follow the density gradient maxima at 450 m. The 27.15 kg/m^3 potential density corresponds to the SAF-M over the continental slope while the slightly lower value (27.10 kg/m^3) corresponds to the SAF downstream of the Confluence with the Brazil Current or Subantarctic Front-Return (hereafter referred to as SAF-R). The lower potential density value of the mean SAF-R is due to the intense mixing with the lighter subtropical waters at the BMC, which decreases (increases) the potential density west (east) of the front (Figure 10 b). The σ_θ=27.00 kg/m^3 isopycnal at 450 m is the best match to the ADT 30 cm contour associated with the BCF (Table 3, Figure 10a, b). However, this isopycnal does not correspond to a maximum density gradient, but rather to the southern limit of the subtropical gyre (Figure 10b). For each front, the mean position inferred from the ADT contours (Table 3, white contours in Figure 10 a) is in close agreement with the mean frontal position inferred from the 450 m potential density criteria (Table 3, heavy contours in Figure 10a).

The Argo float observations at 450 m presented in a Θ–S diagram (Figure 10c) show how the potential density criteria defined from the model outputs mark the transitions between different varieties of water masses. The lighter densities (blue dots) with σ_θ less than 27.00 kg/m^3 correspond to South Atlantic Central Water (SACW) for salinities higher than 34.2 psu and to Subantarctic Surface Water (SASW) for lower salinities. The density range between 27.00 and 27.33 kg/m^3 matches the three varieties of Antarctic Intermediate Water described in section 3.3.1:

AAIW-U (green dots) with 27.00 kg/m^3 < $\sigma\theta$ < 27.15 kg/m^3 and 3°C<T<6°C; a denser colder AAIW-C (yellow dots) with 27.15 kg/m^3 < $\sigma\theta$ < 27.27 kg/m^3 and 2°C < T < 4°C; and a denser and saltier AAIW-L with 27.27 kg/m^3 < $\sigma\theta$ < 27.33 kg/m^3 and 34.2 psu < S < 34.3 psu (orange dots). Finally, waters with densities higher than 27.33 kg/m^3 (red dots) and salinity higher than 34.3 psu correspond to Upper Circumpolar Deep Water (UCDW).

Argo float profiles (10104 profiles for 2007-2016) are classified according to the potential density criteria in Table 3 (Figure 10d). The front locations inferred from Argo floats and the mean location of fronts inferred model potential density at 450 m is quite similar. However, Argo profile locations represented on the same map (e.g. Figure 10d) are not mean but rather instantaneous values, thus different colors coexisting in the same area may indicate the presence of eddies, meanders and other frontal displacements. For example, the presence of orange dots north of the mean PF-N location may be related to sporadic eddies or PF-N meanders within the MC. This is in agreement with the presence of waters derived from the Polar Front, observed at 46 ºS near the center of the cyclonic loop formed by the Malvinas Current and its southward return (Piola and Gordon, 1989). The different colors observed in the C-shaped high EKE region surrounding the western Argentine Basin between the BCF and the SAF-M (Figures 1c, d) are associated with numerous eddies of different densities.

In contrast to drifting Argo floats, the model provides continuous time series of density at any location. Model outputs are now used to examine time variations of the front locations. We examine two zonal sections across the MC, a section at ~51°S over the Malvinas Plateau in the upstream part of the MC crossing the SAF-M, the PF-N and the PF-M, another one more

downstream at ~43°S crossing the SAF-M, the SAF-R and the BCF (red segments in Figures 10 a, b).

4.2 Front variations at 51°S

The section at 51°S crosses the SAF-M (mean location at 54.1°W), the PF-N (mean location at 49.3°W) and the PF-M (mean location at 46.8°W) (Figure 10, Table 4). The section is located over the relatively shallow (< 3000 m) Malvinas Plateau. The mean density increases in the offshore direction at all depths (Figure 11a) and the density standard deviation (Figure 11b) shows a subsurface maximum in the depth range 400 – 1000 m where stratification is important (closely spaced isopycnals in Figure 11a). The subsurface standard deviation maximum is the signature of the mesoscale activity in this region of strong energy dissipation and mixing where the fronts meander and shed eddies (Artana et al., 2016).

Along the section the mean ADT decreases eastward from 17 to -51cm (for both altimetry and the model) and the density increases eastward from 27.10 to 27.37 kg/m^3 (Figure 12 right panels). The standard deviations for each variable (ADT data, ADT model and $\sigma_{\theta 450}$) are quite homogeneous along the section (about 8 cm for ADT and 0.06 kg/m^3 for $\sigma_{\theta 450}$) (Figure 12 right panels). The ratio of the ADT range to the ADT mean standard deviation along the section is about 2, a value similar to the ratio of the density range to the density mean standard deviation.

Time series of ADT (from altimetry and the model) and potential density at 450 m were extracted at the mean location of the fronts. The three time series show a large degree of correlation (> 0.7) for each front (Table 4). Spectra of these time series show similar spectral content for the three variables, except at periods shorter than 15 days, at which the model ADT and $\sigma_{\theta 450}$ have a

significant energy (above 95% confidence level) while the satellite ADT does not, as expected because of the satellite data processing (not shown).

The Hovmöller diagrams of the three variables (ADT data, ADT model and $\sigma_{\theta 450}$) along the section (Figures 12a, b, c) show the time evolution of the three fronts PF-M (yellow contour; ADT = -48 cm and $\sigma_{\theta 450}$ = 27.33 kg/m^3), PF-N (pink contour; ADT = -34 cm and $\sigma_{\theta 450}$ = 27.27 kg/m^3) and SAF-M (black contour; ADT = 0 cm and $\sigma_{\theta 450}$ = 27.15 kg/m^3). As expected, the two ADT Hovmöller diagrams are very similar (Figures 12a, b). The $\sigma_{\theta 450}$ Hovmöller diagram (Figure 12c) mimics the patterns observed in the ADT diagrams. The steric effect, with a typical annual cycle, is not an important component of the sea surface height variability in the region and does not affect the fronts locations. The SAF-M location is somewhat more stable than the PF-N and the PF-M, probably as a result of more effective topographic steering of the flow over the steeper upper slope. Yet the range of variations of the SAF-M location is larger in the density diagram (5° in longitude corresponding to about 300 km at 51°S) than in the ADT diagrams (about 2° in longitude corresponding to about 140 km). The positions of the PF-N and PF-M are highly variable in all diagrams. Tortuous and closed contours between 54°W and 50°W suggest the existence of numerous meanders and eddies as previously reported (Artana et al., 2016).

4.3 Front variations around the MC at 43 °S

The section located at 43°S intersects mean locations of the SAF-M, SAF-R and BCF at 58.3°W, 55.3°W, 54.1°W respectively (Figure 13, Table 4). The mean density field shows reduced isopycnal spacing in the 400-100m depth range and a doming of isopycnals centered around 57°W between the SAF and SAF-R mean positions (Figure 13a). The density standard deviation (Figure

13b) features large values at all depths on the eastern side of the section associated with the high EKE region shown in Figure 1d.

Along the section the mean ADT (satellite and model) varies between -22 and 35 cm with a minimum at 57°W associated with the center of the cyclonic loop between the MC and its return flow (Figure 14, panels to the right). The mean potential density at 450 m ranges between 27.10 and 27.22 kg/m^3 with a maximum at 57°W, matching the location of the low ADT. This reflects the low sea level and upward doming of isopycnals at the core of the cyclonic trough. The standard deviation in ADT (potential density) increases eastward from 3 cm to 31 cm (0.02 kg/m^3 to 0.13 kg/m^3) respectively (Figure 14, right hand side panels).

The time series of ADT (satellite and model) and of $\sigma\theta_{450}$ extracted at each front location are highly correlated (r>0.6, Table 4). The time series extracted at the SAF-R moderately co-vary with the time series extracted at the BCF in the three fields (r~0.4). For each front, the spectra of the three time series at 43°S (not shown) present similar characteristics except at high frequencies (periods less than 15 days) where satellite ADT does not present any significant energy. The model variables show more high-frequency variations as expected from the model higher spatial resolution and higher EKE.

The Hovmöller diagrams of the satellite ADT, model ADT and potential density at 450 m from 2007 to 2016 along the section at 43°S (Figures 10a, b; 14a, b, c) show the temporal evolution of the SAF-M (white contour), SAF-R (ADT = 0 cm, $\sigma\theta_{450}$ = 27.10 kg/m^3, blue contour) and BCF position (ADT = 30 cm, $\sigma\theta_{450}$ = 27.00 kg/m^3, brown contour). The range of variation of the SAF location is quite small (1° in longitude in the satellite and model ADT, and 1.5° in the potential

density at 450 m). The SAF-M location is strongly controlled by the continental slope and remains close to its mean location. The location of the SAF-R is much more variable and generally co-varies with the BCF location (Figure 14). The range of SAF-R variations is about 2° in longitude in the ADT and about 3° in longitude in the potential density. The BCF presents larger excursions in the potential density diagram than in ADT (data or model). Several times the $\sigma\theta_{450}$-inferred BCF extends beyond 56°W while the ADT-inferred BCF never reaches this longitude.

The potential density diagram at 450 m shows a few episodes of particularly low density (~27.10 kg/m^3) at 57°W (for instance in April 2013). Vertical density sections and maps of density at 450 m and ADT (example in Figure 15a, b, c) from a model snapshot in mid-April 2013 reveal that these extreme events correspond to an invasion of the Brazil Current over the section. Isopycnals corresponding to the AAIW water mass varieties (between 27.00 and 27.35 kg/m^3) are found at a deeper level than their mean location (Figure 15a and 13a) and corresponding ADT maps show the invasion of the Brazil Current (Figure 15b). The sinking is more easily observed in the density field than in the ADT field (Figure 15c). About 4 such events are detected in the 10 year time series. During those events the location of the SAF-M in the ADT and $\sigma\theta_{450}$ maps is different north of 44°S (Figure 15b and c).

Between 58°W and 55°W, the ADT and potential density time series display closed contours corresponding to the PF-M and PF-N (pink and yellow contours in Figure 14c) which are associated with cyclonic mesoscale structures. An example is shown in the model snapshot of 4 June 2012 (Figure 15d, e, f). All isopycnals are shallower than in the mean potential density section (Figure 15 d and 13a). Specifically, the 27.27 kg m^{-3} isopycnal associated with the PF-N rises above 450 m between 57.7 and 57.0°W (Fig. 15d). The corresponding map of potential density at

450 m shows that the doming is part of a rather large structure extending over 4 degrees in latitude and 1 to 2 degrees in longitude (Figure 15f). The signature of the structure is quite weak in the ADT map (Figure 15e). This structure has been tracked back in time in the density maps. It originates from a meander of the Polar Front that shed a large cyclonic eddy around 16 April 2013 over the Malvinas Plateau. The eddy northward progression (at a speed of about 10 km/day closely follows the 2000 m) can be tracked in the density maps. The eddy is seen in the ADT maps close to its formation, but its signature is lost after leaving the Malvinas Plateau (not shown).

4.4 Loci of the PF-N and PF-M: differences between ADT and potential density at 450m.

The PF-M and PF-N contours are more numerous in the potential density field at 450 m than in the ADT field (Figure 14 a, b c). The PF-N and PF-M positions of 10 years of model snapshots (sampled every 5 days for sake of clarity) from ADT and potential density at 450 m show some interesting differences (Figure 16). North of the Malvinas Plateau (north of 48°S), the Polar Front contours, whether derived from ADT or from potential density at 450 m, tend to be closed. This suggests the occurrence of eddies shed by the PF north of 48°S. The ADT-derived Polar Front (PF-N and PF-M) contours tend to veer offshore towards the deep Argentine Basin and do not reach the continental slope onshore of the 3000 m isobath. In contrast, several Polar Front contours derived from the potential density at 450 m extend on the continental slope along the MC path, with PF-M contours found more on the outer slope (depths > 2000m).

The potential density field at 450 m is able to better detect eddies shed by the PF-M and PF-N over the continental slope than the ADT. Contrasts between water masses are more evident in the potential density field at 450 m than in the ADT because Polar Front waters in the MC trough are associated with subsurface intrusions of relatively cold and fresh anomalies (Piola and Gordon, 1989). Since sea surface height variations reflect integrated changes over the full-depth water

column, relatively weak and small-scale features in the density field may not be detected in ADT field.

In contrast, the ADT depicts eddies shed by the PF crossing the Malvinas Escarpment and entrained northeastward into the energetic circulation over the deep Argentine Basin while the signature of those eddies is lost in the potential density field at 450 m. The stretching of eddies as they are drawn into the deep Argentine Basin and cross the steep slope of the Malvinas Escarpment most likely modifies their vertical structure and their potential density at 450m. The typical potential density values associated with the PF branches at 450 m (Table 3) are plausibly found on a deeper level. A precise examination of the process is beyond the scope of this work.

The ADT and potential density at 450 m provide non-identical and complementary information on eddies shed by the Polar Front: while ADT depicts the surface geostrophic circulation with PF eddies entrained in energetic circulation over the deep Argentine Basin, potential density at 450 m is more effective at monitoring PF eddies feeding the Malvinas Current.

5. **Summary and conclusion**

The performance of the Mercator Ocean global operational system PSY4 in the Southwestern Atlantic Ocean has been evaluated using 10 years of satellite data and Argo floats (PSY4 assimilates along-track altimetric data, SST and Argo float data) and one year of independent mooring data deployed in the MC in the vicinity of the BMC.

Comparisons with satellite gridded data over the 2007-2016 period show that the model produces realistic circulation patterns in the region. The model EKE is generally higher than the altimetric EKE over the Argentine Basin (e.g. by up to 400 cm^2/s^2 in the BMC). We postulate that the

increased model EKE is due to the increased spatial resolution of the model grid (1/12°), which resolves mesoscale features that are not captured by present satellite altimetry processing. The comparison of model outputs collocated in time and space with Argo floats profiles show that the model also reproduces some of the complex hydrographic features of the study area. Two specific Argo floats providing daily profiles illustrate the performance of the operational model in the Malvinas Current system.

The performance of the model is particularly satisfactory in the Brazil Malvinas Confluence. The comparison is a stringent test for model performance because the BMC presents a complex water mass structure and dynamics. Model outputs were also compared to *in situ* temperature, salinity, density and velocity observations gathered at three moorings deployed from December 2014 to November 2015 at 41°S. Despite the fact that this observation period presents outstanding variability in the intensity of the MC (Artana et al., 2018) and the regional eddy kinetic energy (Ferrari et al., 2017), the model hydrographic property distributions and velocity fields present a good agreement with the in-situ and satellite altimeter observations. The model water mass structure at 41°S is consistent with previous descriptions (Maamaatuaiahutapu et al., 1994). At this location the model outputs accurately match the mean and standard deviation of the *in situ* temperature, salinity and density. Over the upper slope the agreement between model outputs and 10-day low pass-filtered *in situ* velocity time series is remarkable. The model reproduces the strong and weak regimes of the MC that characterized the mooring period (Ferrari et al., 2017). However, in June 2015 model velocities significantly depart from *in situ* data. The time series of the difference between model SLA and altimetric SLA presents large values (>25 cm) during June 2015, at a time of an exceptionally weak Malvinas Current. The BMC region at that time was mostly cloud-covered and uncertain SST data seem to have prevailed over the altimetric data in

the assimilation scheme. Except for the above-mentioned deviations of the model in June 2015, which are unique during the entire 10 years of model outputs, the performance of the model close to the BMC region is remarkably good.

The location of the fronts of the MC system corresponds to large gradients in ADT and in potential density at 450 m. We identified values in ADT and potential density at 450 m that match the mean potential density gradients. For each front, the mean position inferred from the ADT coincides with the mean position inferred from the 450 m potential density field. We used these ADT values to monitor the variations of the location of the fronts over two sections crossing the MC. The section at 51°S over the Malvinas Plateau, crosses the SAF-M, PF-N, and PF-M, and the section at 43°S, crosses the SAF-M, the SAF-R, and the BCF. The variations in the front locations in the three fields (satellite ADT, model ADT and model potential density at 450 m) present a good agreement.

Nevertheless, the PF-N and PF-M positions of 10 years of model snapshots from ADT and potential density at 450 m show some interesting differences. The potential density field at 450 m is useful to detect and track eddies shed by the PF-M and PF-N that feed the MC and have a much weaker signal in the ADT. In contrast, the ADT depicts eddies shed by the PF crossing the Malvinas Escarpment and entrained into the energetic circulation over the deep Argentine Basin while the signature of those eddies is lost in the potential density field at 450 m.

Acknowledgments:

The authors are grateful to the CNES (Centre National d'Etudes Spatiales) for constant support. This study is a contribution to EUMETSAT/CNES DSP/OT/12-2118. Camila Artana under Ph.D. Scholarship from Sorbonne Université. The satellite data and model outputs are available at Copernicus Marine Environment Monitoring Service (CMEMS; http://marine.copernicus.eu/) and the in situ data are available at SEANOE (www.seanoe.org; Saraceno et al, 2017). The float data were collected and made freely available by the international ARGO program and the national programs that contribute to it (http://www.argo.ucsd.edu). The ARGO program is part of the Global Ocean Observing System. We are grateful to the editor Don Chambers and to two anonymous reviewers for a number of constructive comments and suggestions.

References

Argo Data Management (2013), *Argo Quality Control Manual Version 2.9*, 54 pp.

Artana, C., R. Ferrari, Z. Koenig, M. Saraceno, A. R. Piola, and C. Provost (2016), Malvinas Current variability from Argo floats and satellite altimetry, *J. Geophys. Res. Oceans*, 121, 4854–4872, doi:10.1002/2016JC011889.

Artana C., R. Ferrari, Z. Koenig, N. Sennéchal, M. Saraceno, A.R. Piola and C. Provost (2018), Malvinas Current volume transport at 41°S: a 24-year long time series consistent with mooring data from 3 decades and satellite altimetry, *J. Geophys. Res. Oceans*, 122, doi: 10.1002/2017JC013600

Barré N., C. Provost, A. Renault, and N. Sennéchael (2011), Fronts, meanders and eddies in Drake Passage during the ANT-XXIII/3 cruise in January-February 2006 : a satellite perspective. *Deep Sea Res.*, part II, 58, 2533-2554. doi :10.1016/j.dsr2.2011.01.003.

Cabanes, C., Grouazelm A., vos Schuckmann, K., Hamon, M., Turpin, V., Coatanoan, C., Paris, F., Guinehut, S., Boone, C., Ferry, N., de Boyer Montegut, C., Carval, T., Reverdin G., Pouliquen, S., Le Traon, P.Y., (2013), The CORA dataset: validation and diagnostics of in-situ ocean temperature and salinity measurements. *Ocean Sci.* 9, 1-18. Doi:10.5194/os-9-1-2013.

Combes, V., and R. P. Matano (2014), A two-way nested simulation of the oceanic circulation in the Southwestern Atlantic, *J. Geophys. Res.* Oceans, 119, 731–756, doi:10.1002/ 2013JC009498.

Donlon, C.J., Martin, M., Stark, J., Roberts-Jones, J., Fiedler, E., Wimmer, W., (2012). The Operational Sea Surface Temperature and Sea Icea Analysis (OSTIA) system. *Remote Sensing of Environment* 116, 140-158. doi: 10.1016/j.res.2010.10.017.

Ferrari R., C. Artana, M. Saraceno, A.R. Piola, and C. Provost (2017), Satellite altimetry and current-meter velocities in the Malvinas Current at 41°S: comparisons and modes of variations, *J. Geophys. Res.*, Oceans. doi: 10.1002/2017JC013340.

Jia, W., D. Wang, N. Pinardi, S. Simoncelli, A. Storto, S. Masina (2016), A Quality Control Procedure for Climatological Studies Using Argo Data in the North Pacific Western Boundary Current Region, *J. Atmos. Oceanic Technol*., 33, pp. 2717 – 2733. doi:10.1175/JTECH-D-15-0140.1

Lellouche J.-M., O. Le Galloudec, M. Drévillon, C. Régnier, E. Greiner, G. Garric, N. Ferry, C. Desportes, C.E. Testut, C. Bricaud, R. Bourdallé-Badie, B. Bourdall, M. Tranchant, Y. Benkiran, A. Drillet, A. Daudin, C. De Nicola (2013), Evaluation of real time and future global monitoring and forecasting systems at Mercator Ocean, *Ocean Sci. Discuss.*, 9, 1123–1185.

Lellouche, J.-M., Greiner, E., Le Galloudec, O., Garric, G., Regnier, C., Drevillon, M., Benkiran, M., Testut, C.-E., Bourdalle-Badie, R., Gasparin, F., Hernandez, O., Levier, B., Drillet, Y., Remy, E., and Le Traon, P.-Y. (2018), Recent updates on the Copernicus Marine Service global ocean monitoring and forecasting real-time 1/12° high resolution system, Ocean Sci. Discuss., https://doi.org/10.5194/os-2018-15.

Madec, G. (2008), NEMO ocean engine. Note du Pôle de modélisation, Institut Pierre-Simon Laplace (IPSL), France, No. 27 ISSN, 1288-1619.

Maamaatuaiahutapu, K., V.C. Garcon, C. Provost, M. Boulhadid, A.A. Bianchi, (1994), Spring and winter water mass composition in the Brazil-Malvinas Confuence. *J. Mar. Res*. 52, 397-426.

Mc Cartney M.S. (1977), Subantarctic Mode Water, Deep Sea Res., 24, supplement, 103-119.

Nowlin, W. D., Jr., T. Whitworth III, and R. D. Pillsbury (1977), Structure and transport of the Antarctic Circumpolar Current at Drake Passage from short-term measurements, *J. Phys. Oceanogr.*, 7(6), 788–802.

Orsi, A. H., I. T. Whitworth, and J. W. Nowlin (1995), On the meridional extent and fronts of the Antarctic Circumpolar Current, *Deep Sea Res.*, Part I, 42, 641–673, doi:10.1016/0967-0637(95)00021-W.

Piola A.R. and D.T. Georgi, (1982), Circumpolar properties of Antarctic Intermediate Water and Subantarctic Mode Water. Deep-Sea Research, 29 (1982), pp. 687-712

Piola A.R. and A.L. Gordon, (1989), Intermediate waters in the southwest South Atlantic. *Deep Sea Res*., vol 36, 1, 1-16.

Piola, A. R., B. C. Franco, E. D. Palma, and M. Saraceno (2013), Multiple jets in the Malvinas Current, *J. Geophys. Res. Oceans*, 118, 2107–2117, doi:10.1002/jgrc.20170.

Provost C., S. Gana, V. Garçon, K. Maamaatuaiahutapu, and M. England, (1995), Hydrographic Conditions in the Brazil Malvinas Confluence during austral summer 1990. *J. Geophys. Res., Oceans*, 100, C6, 10,655-10,678.

Provost, C., A. Renault, N. Barré, N. Sennéchael, V. Garçon, J. Sudre, and O. Huhn (2011), Two repeat crossings of Drake Passage in austral summer 2006: Short-term variations and evidence for considerable ventilation of intermediate and deep waters, *Deep Sea Res.*, Part II, 58(25), 2555–2571, doi:10.1016/j.dsr2.2011.06.009.

Pujol, M.-I., Y. Faugère, G. Taburet, S. Dupuy, C. Pelloquin, M. Ablain, and N. Picot, (2016), DUACS DT2014: the new multi-mission altimeter data set reprocessed over 20 years, *Ocean Sci*., 12, 1067-1090, doi:10.5194/os-12-1067-2016.

Rio, M.-H., Mulet, S. and Picot, N. (2014), Beyond GOCE for the ocean circulation estimate: Synergetic use of altimetry, gravimetry, and in situ data provides new insight into geostrophic and Ekman currents, Geophys. Res. Lett., 41, doi:10.1002/2014GL061773.

Roden, G. I. (1986), Thermohaline fronts and baroclinic flow in the Argentine basin during the austral spring of 1984, J. Geophys. Res., 91(C4), 5075–5093, doi:10.1029/JC091iC04p05075.

Saraceno M., R. Guerrero, A. R. Piola, C. Provost, F. Perault, R. Ferrari, G. Paniagua, L. Lago, C. Artana (2017). Malvinas Current 2014-2015: Mooring velocities. SEANOE. doi.org/10.17882/51492.

Smith, W. H. F., and D. T. Sandwell (1994), Bathymetric prediction from dense satellite altimetry and sparse shipboard bathymetry, *J. Geophys. Res.*, 99, 21 803–21 824.

Sokolov, S., and S. R. Rintoul (2009a), The circumpolar structure and distribution of the Antarctic Circumpolar Current fronts. Part 1: Mean circumpolar paths, *J. Geophys. Res.*, 114, C11018, doi:10.1029/2008JC005108.

Sokolov, S., and S. R. Rintoul (2009b), Circumpolar structure and distribution of the Antarctic Circumpolar Current fronts: 2. Variability and relationship to sea surface height, *J. Geophys. Res.*, 114, C11019, doi:10.1029/2008JC005248.

Szekely, T., Gourrion, J., Pouliquen, S., Reverdin, G., 2016. CORA, Coriolis, Ocean Dataset for Reanalysis. SEANOE doi:/http://doi.org/10.17882/46219.

Vivier, F., and C. Provost (1999), Direct velocity measurements in the Malvinas Current, *J. Geophys. Res. Oceans,* 104, 21,083–21,103, doi:10.1029/ 1999JC900163.

Figure caption:

Figure 1:

Mean surface velocity magnitude (in cm/s) and mean surface velocities (larger than 10 cm/s) from gridded altimetry (a) and from model outputs (c). Mean eddy kinetic energy per unit mass (in cm^2/s^2) from gridded altimetry (b) and from model outputs (d) for the 2007-2016 period. Bottom topography isobaths correspond to 6000, 5000, 3000, 1000 and 300 m (from Smith and Sandwell, 1994). The mean locations of the main Antarctic Circumpolar Current (ACC) fronts as defined by Barré et al. (2011) are plotted: Subantarctic Front (SAF), in black (SAF-M solid line and SAF-N dashed line); Polar Front (PF), in red (PF-M solid line and PF-N and PF-S dashed line); and Southern ACC (SACCF) in grey (SACCF-N and SACCF-S in dashed lines). The mean position of the Brazil Current Front (BCF, solid light blue) is from Ferrari et al., 2017. The red line indicates a segment of the Jason satellite track #26. The 0 km is refered to the 300 m isobat. The instruments on the 2014-2015 moorings are represented with red diamonds in e). EBB: East of Burdwood Bank, DP: Drake Passage, NSR: North Scotia Ridge.

Figure 2

Salinity (psu), potential temperature (°C), and potential density (kg/m^3) at 450 m depth from Argo float profiles over the 2007-2016 period (a,b,c). Mean salinity (psu), potential temperature (°C) and potential density (kg/m^3) at 450 m depth over 2007-2016 from model outputs (d,e,f). Isobaths as in Figure 1

Figure 3:

a. Trajectory of Argo float 1 (platform number 6901650) colored as a function of time. Daily potential temperature profiles from the Argo float (b) and collocated model outputs (c) as a function

of time. Black crosses in panel a indicate the float position at the dates indicated with vertical lines in panels b and c.

d. Trajectory of Argo float 2 (platform number 6901654) colored as a function of the observed salinity at 30 m. Isobaths as in Figure 1. e (f) salinity profiles from the Argo float (model outputs) with a daily resolution. Shallow topography appears in white. The x-axis is latitude. The y-axis is the depth (in m).

Figure 4:

Mean (a,b,c) and standard deviation (d,e,f) of temperature (°C), salinity (psu) and density (kg/m^3) from model outputs (December 2014-November 2015) along the 160 km-long section marked in red in Figure 1. Corresponding values from observations at each instrument are indicated by colored dots. The depth scale of the y-axis is stretched in the upper 2000 m.

Figure 5:

Mean (a,b) and standard deviation (c,d) of the along-slope (top panels) and across-slope (bottom panels) velocity components from model outputs (December 2014-November 2015) along the 160 km-long section (from west to east) marked in red in Figure 1. Corresponding values from observations at each instrument are indicated by colored dots. The depth scale of the y-axis is stretched in the upper 2000m.

Figure 6:

Along-slope (a and b) and across-slope (c and d) velocity time series recorded by the ADCP (left panels) and from model outputs (right panels) interpolated at the ADCP position during the mooring period (December 2014-November 2015).

Along-slope and across-slope velocity time series at 328 m from the ADCP (e) and from model outputs interpolated at the instrument position (f) for the mooring period (December 2014-November 2015).

Figure 7:

Hovmöller diagram of SLA (cm) along a 160 km-long section marked in red in Figure 1c (Jason track #26) based on the along-track altimetric product from December 2014 to December 2015 (a) and from model outputs along the same track (b). Difference between along-track SLA and model SLA (c). (d) Hovmöller diagram of the satellite minus model SLA over the same track #26 extended over the 10-year period of model availability (2007-2016).

Figure 8:

ADT distributions (in cm) from gridded altimetric products (a) and model outputs (b) for 10 June 2015. The along-track altimetric product (from Altika and Cryosat satellites) for the week centered on this date is superimposed. The differences between the gridded maps and the along-track altimetric product are shown in c and d. SST distributions (°C) from OSTIA (e) and from model outputs (f) for 10 June 2015. The black contour is the 10°C isotherm which corresponds to the location of the maximum SST gradient for that day. The black line indicates the position of Jason track #26. The position of the 2014-2015 moorings is indicated with green markers. Isobaths as in Figure 1.

Figure 9:

(a) Mean ADT gradient in cm/100 km from gridded altimetry and (b) mean ADT (in cm). (c) mean potential density gradient at 540 m in kg/m^3/100 km from model outputs and (d) mean potential density (kg/m^3) at 540 m (e) mean potential density gradient at 380 m in kg/m^3/100 km from model

outputs and (f) mean potential density (kg/m^3) at 380 m The heavy black contours corresponding to specific fronts from Table 3. Isobaths as in Figure 1

Figure 10

(a) mean potential density gradient at 450 m in kg/m^3/100 km from model outputs and (b) mean potential density (kg/m^3) at 450 m . The heavy black contours correspond to specific fronts from Table 3. The thin white lines are the ADT contours of Figure 9a.

(c) Potential temperature-salinity diagram from Argo float data at 450 m classified in terms of potential density criteria at 450 m (Table 3). Corresponding water masses are indicated. (d) Location of the Argo float profiles over 2007-2016. The color code corresponds to the potential density at 450 m as in (c). The heavy black contours are the potential densities isolines from (b). Isobaths as in Figure 1.

Figure 11:

Mean density (a) and standard deviation (b) of potential density along the zonal section at 51°S (red line in Figure 10a). The mean position of SAF-M, PF-N and PF-M and the 450 m depth are indicated with green and red lines respectively.

Figure 12:

Hovmöller diagrams of satellite gridded ADT (in cm) (a), model ADT (in cm) (b) and model potential density (in kg/m^3) at 450 m along a zonal section (red line in Figure 10 a) at ~51°S over the Malvinas Plateau. The mean locations of the SAF-M (54.1°W), the PF-N (49.3°W) and the PF-M (47.8°W) are indicated in each panel with horizontal lines. The isolines corresponding to the SAF-M are in black, to PF-N in pink and to PF-M in yellow. Right panels show the mean

value of each variable plotted along the section and the shaded area represents the standard deviation.

Figure 13:

Mean density (a) and standard deviation (b) of density along the zonal section at 43°S (red line in Figure 10a). The mean position of SAF-M, SAF-R and BCF and the 450 m depth are indicated with green and red lines respectively.

Figure 14:

Hovmöller diagrams of satellite gridded ADT (in cm) (a), model ADT (in cm) (b) and model potential density (in kg/m^3) at 450 m along a zonal section (red line in Figure 10 a) at ~43°S. The mean locations of the SAF-M (58.3°W), the SAF-R (55.3°W) and the BCF (54.1°W) are indicated in each panel with horizontal lines. The isolines corresponding to the SAF-M are in white, to SAF-R in blue and to BCF in brown. In each panel the pink and yellow contours correspond to PF-N and PF-M. The two vertical black lines mark the dates that are shown in Figure 15. Right panels show the mean value of each variable plotted along the section and the shaded area represents the standard deviation.

Figure 15:

a) Model potential density section at 43°S on 14 of April 2013. The green vertical lines indicate the mean location of the SAF-M, SAF-R and BCF (from Figure 9a). The thick white arrows near the surface indicate the location of the SAF-M and SAF-R according to ADT. 450 m depth is marked with a red line and dashed white lines are the selected isopycnals indicated in Table 3.

b) and c) model ADT and density maps for the 14 of April 2013.

d) same as a) for the 4 of June 2012. The white vertical lines indicate the location of the SAF-M, PF-N and SAF-R inferred front potential density at 450 m as labelled.

e) and f) model ADT and density maps for the 4 of June 2012.

Figure 16:

Loci of PF-N and PF-M from 10 years of model snapshots (sampled every 5 days).

a)Positions of PF-N from ADT

b)Positions of PF-N from potential density at 450 m

c) Positions of PF-M from ADT

d) Positions of PF-M from potential density at 450 m

Table caption:

Table 1. Comparisons between mooring data (December 2014-November 2015) and collocated model outputs (Mean (μ) and standard deviation (σ) and root mean square difference anomaly rmsda). Temperature (T, °C), salinity (S, psu) density (D, kg/m^3), along-slope velocity (V//, cm/s) and across-slope velocity (V$^{\perp}$, cm/s).

Table 2. Potential density characteristics of the main water masses in the region as defined by Maamaatuaiahutapu et al. (1994). SASW: Subantarctic Surface Water; SACW: South Atlantic Central Water; AAIW: Antarctic Intermediate Water -U upper, -C Central, -L Lower; UCDW: Upper Circumpolar Deep Water; CDW Common Deep Water; LCDW Lower Circumpolar Deep Water.

Table 3. Values of ADT and Potential Density at 380m, 450 m and 540 m associated with the main fronts in the MC system.

Table 4.

Correlation (R) between time series of ADT (from satellite altimeter and model) and potential density at 450 m at the mean front location.

Figures:

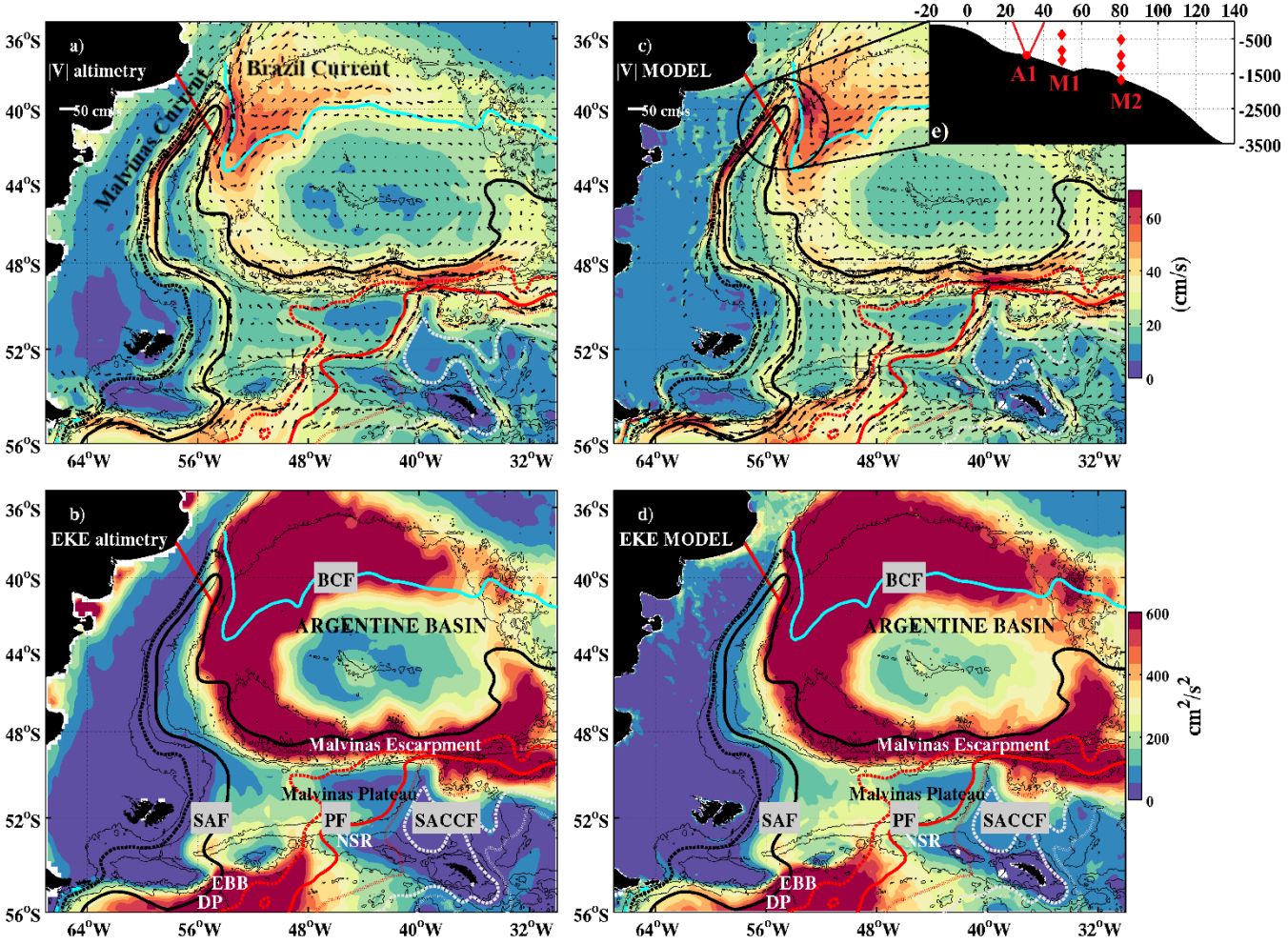

Figure 1

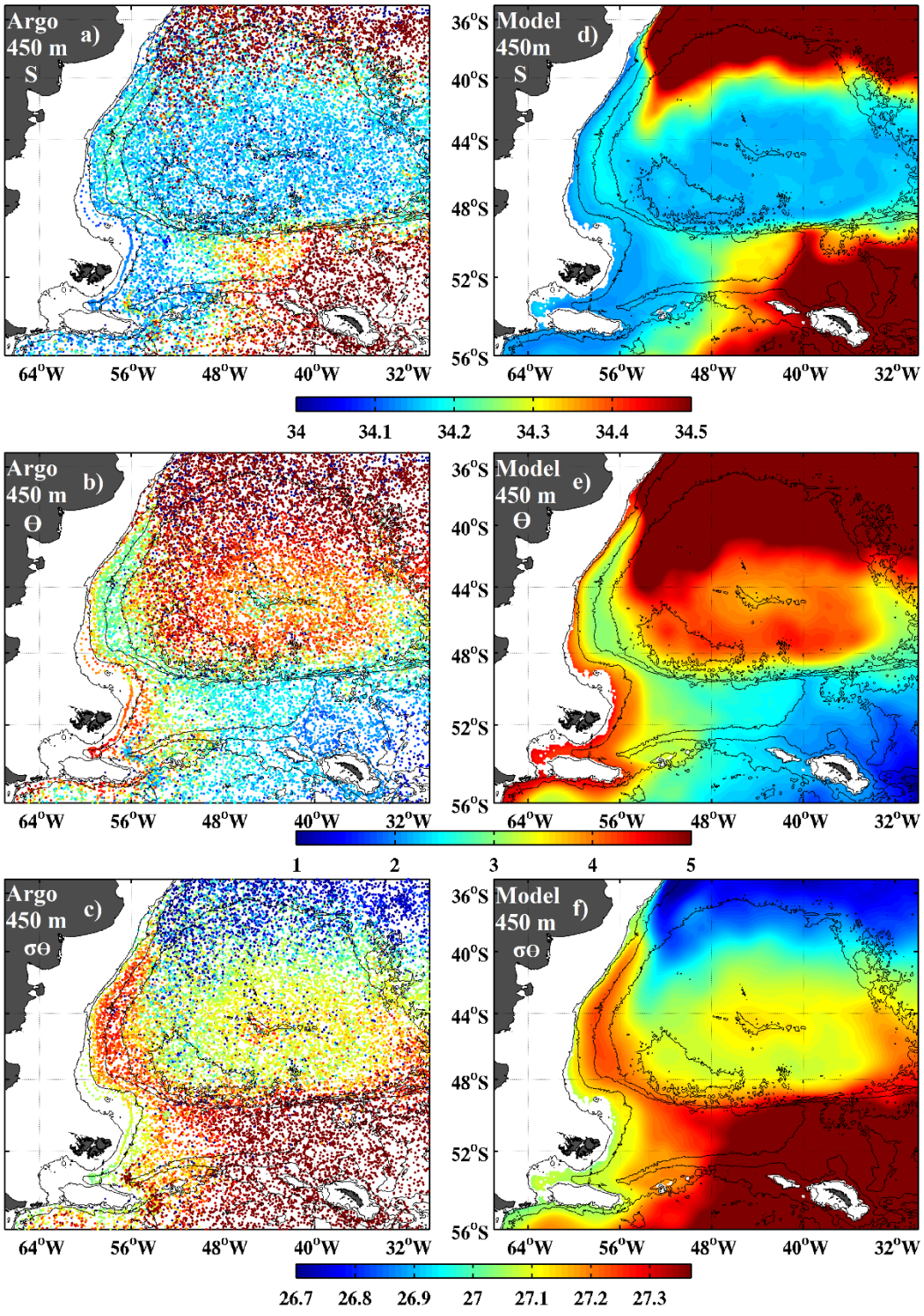
Argo
450 m
S
a)
Model
450m
S
d)
Argo
450 m
Θ
b)
Model
450 m
Θ
e)
Argo
450 m
σΘ
c)
Model
450 m
σΘ
f)
36°S
40°S
44°S
48°S
52°S
56°S
64°W
56°W
48°W
40°W
32°W
34
34.1
34.2
34.3
34.4
34.5
1
2
3
4
5
26.7
26.8
26.9
27
27.1
27.2
27.3

Figure 2

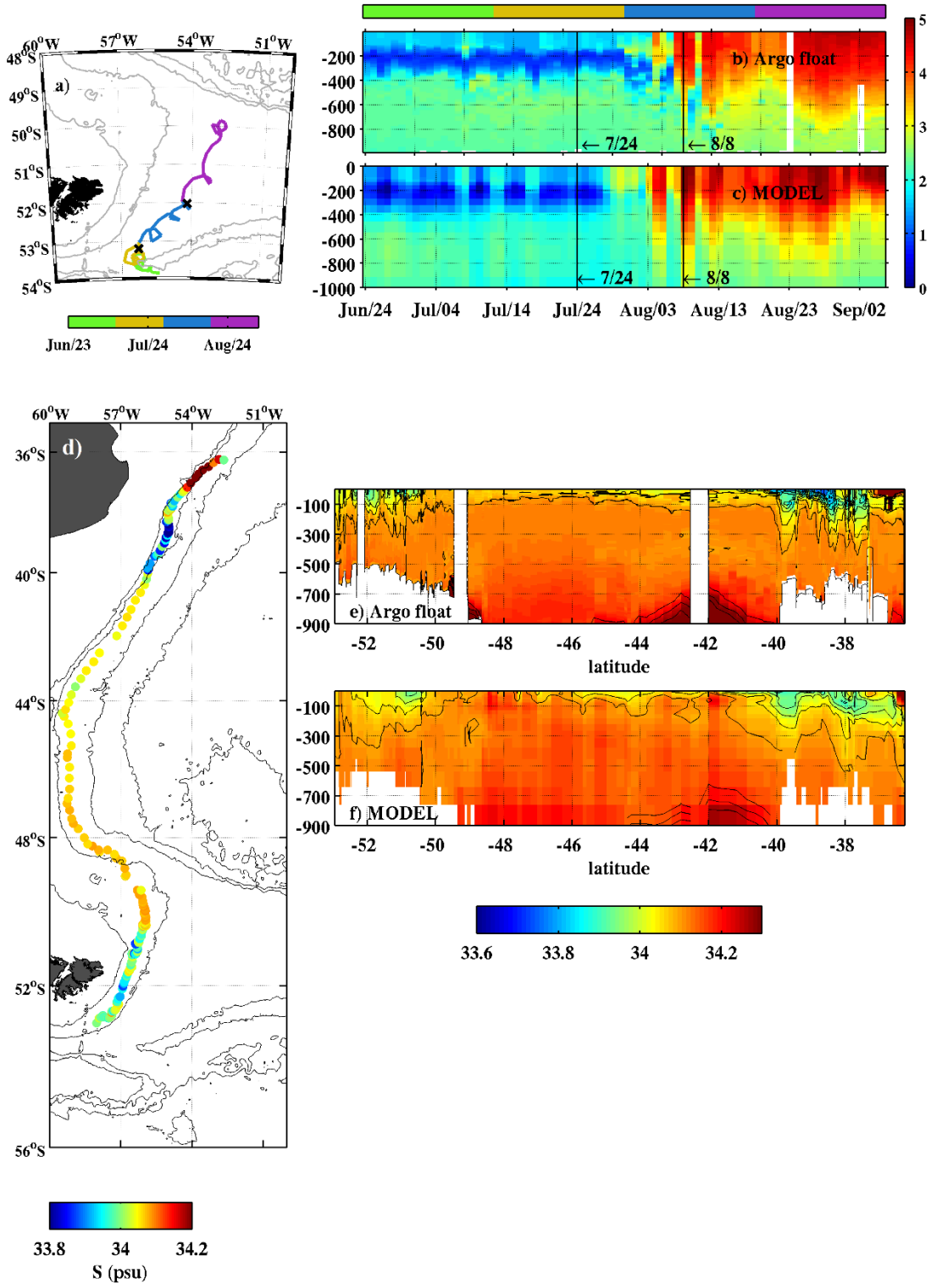
60°W
57°W
54°W
51°W
48°S
49°S
50°S
51°S
52°S
53°S
54°S
a)
Jun/23
Jul/24
Aug/24
b) Argo float
c) MODEL
← 7/24
← 8/8
-200
-400
-600
-800
-1000
0
Jun/24
Jul/04
Jul/14
Jul/24
Aug/03
Aug/13
Aug/23
Sep/02
5
4
3
2
1
0
d)
36°S
40°S
44°S
48°S
52°S
56°S
33.8
34
34.2
S (psu)
e) Argo float
f) MODEL
-100
-300
-500
-700
-900
-52
-50
-48
-46
-44
-42
-40
-38
latitude
33.6
33.8
34
34.2

Figure 3

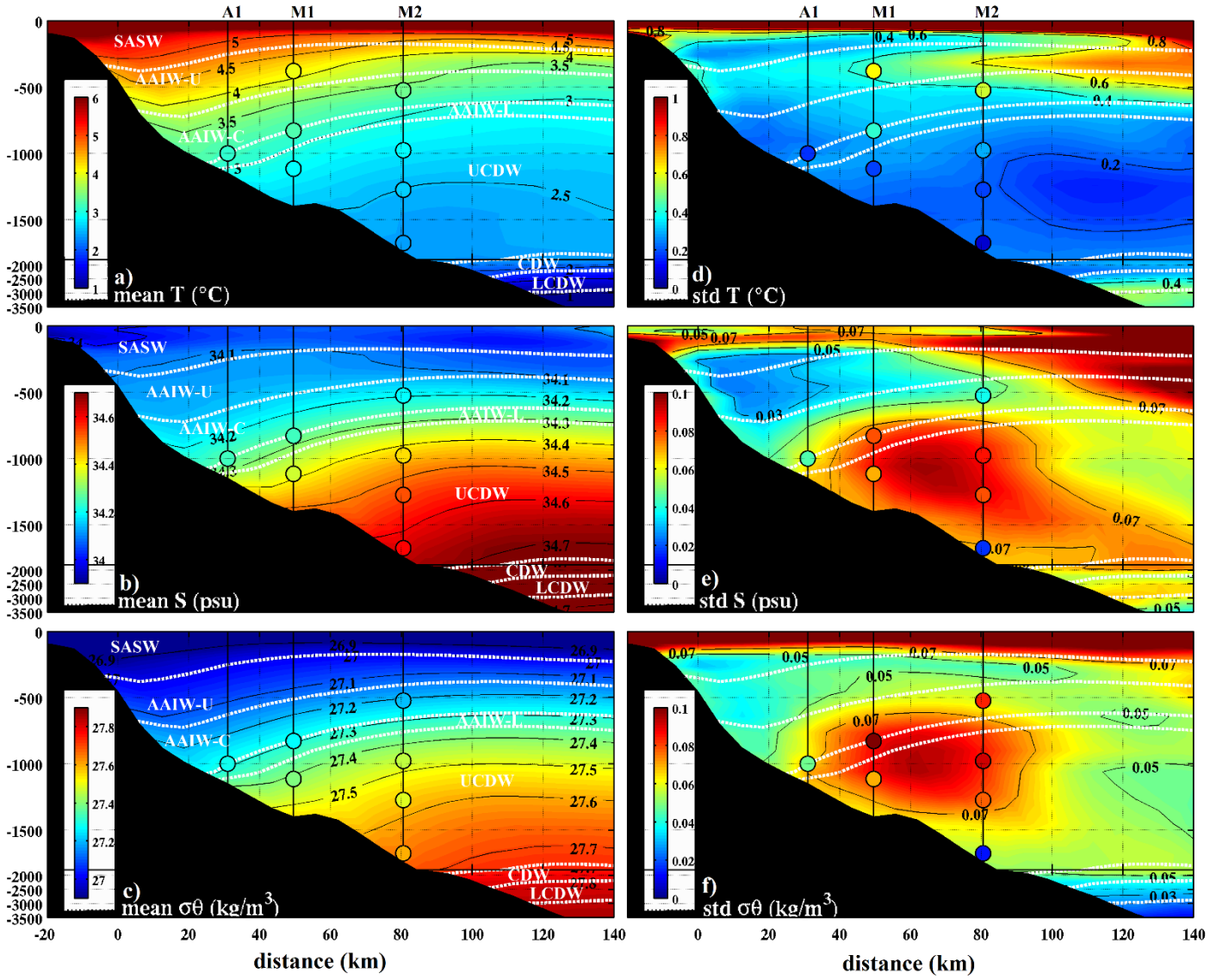
A1
M1
M2
SASW
AAIW-U
AAIW-C
AAIW-I
UCDW
CDW
LCDW
a)
mean T (°C)
b)
mean S (psu)
c)
mean σθ (kg/m3)
d)
std T (°C)
e)
std S (psu)
f)
std σθ (kg/m3)
distance (km)
distance (km)

Figure 4

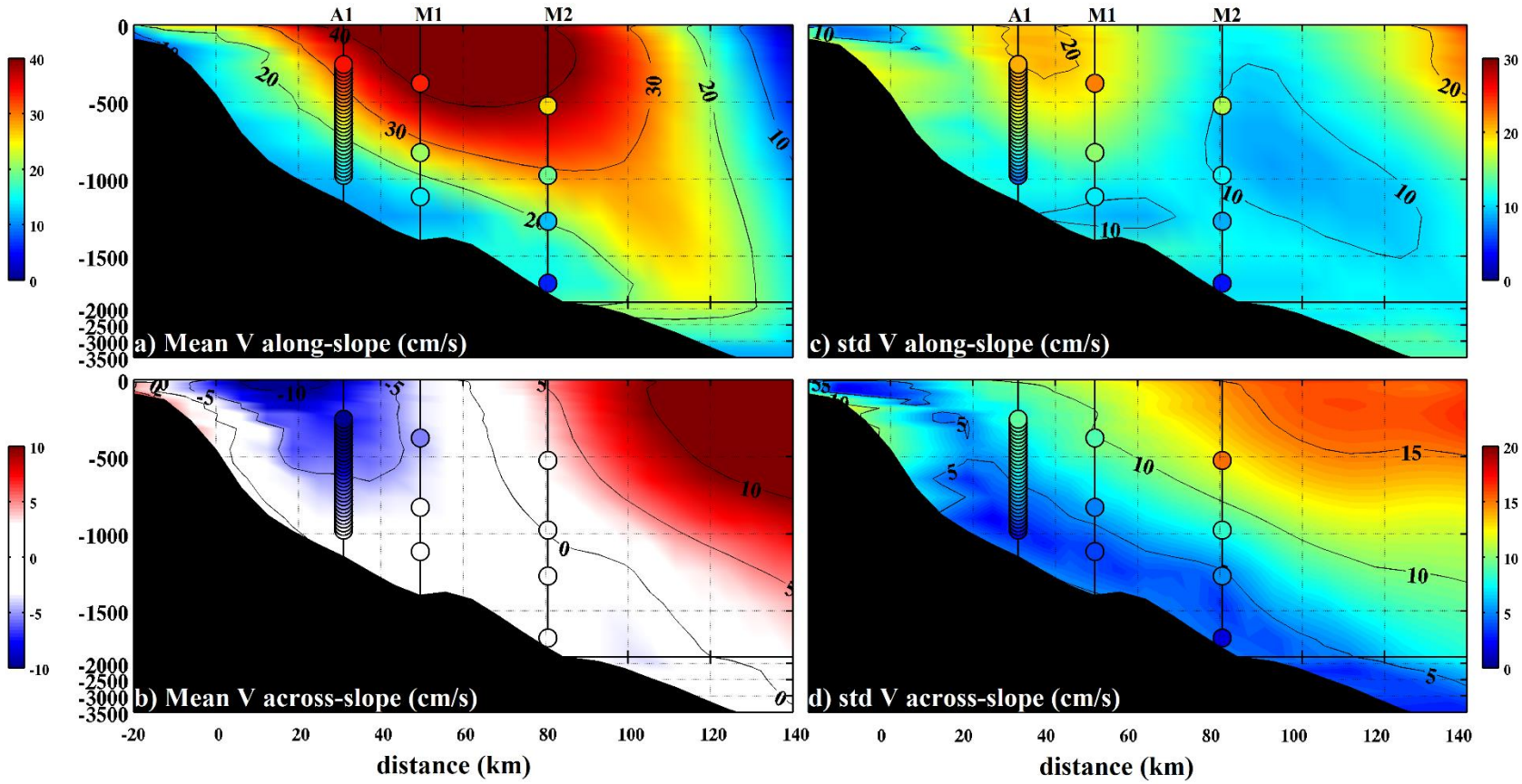
A1
M1
M2
a) Mean V along-slope (cm/s)
b) Mean V across-slope (cm/s)
c) std V along-slope (cm/s)
d) std V across-slope (cm/s)
distance (km)
distance (km)

Figure 5

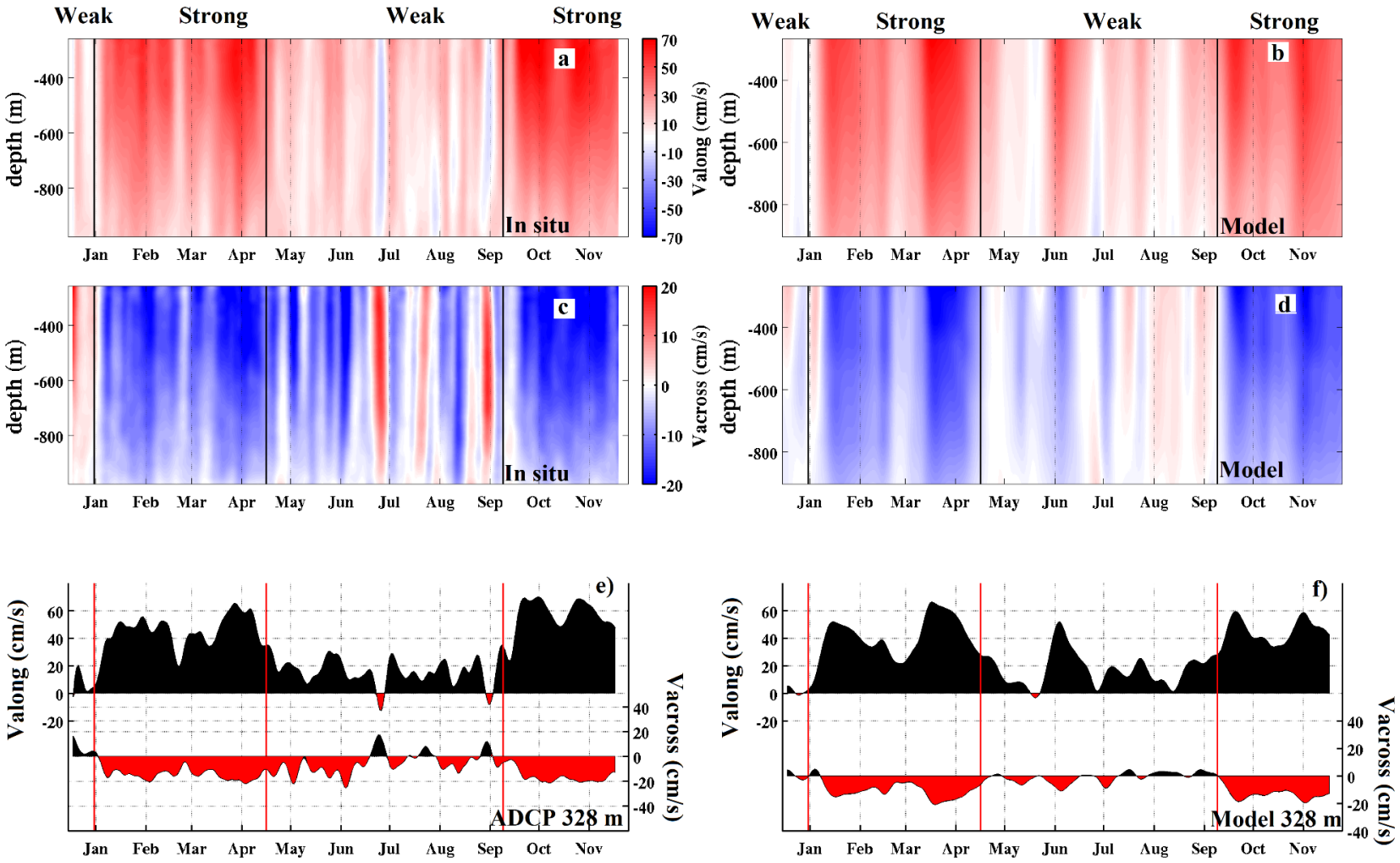
Weak
Strong
Weak
Strong
a
In situ
b
Model
c
In situ
d
Model
depth (m)
-400
-600
-800
Jan
Feb
Mar
Apr
May
Jun
Jul
Aug
Sep
Oct
Nov
Valong (cm/s)
70
50
30
10
-10
-30
-50
-70
Vacross (cm/s)
20
10
0
-10
-20
e)
f)
ADCP 328 m
Model 328 m
60
40
20
0
-20
-40

Figure 6

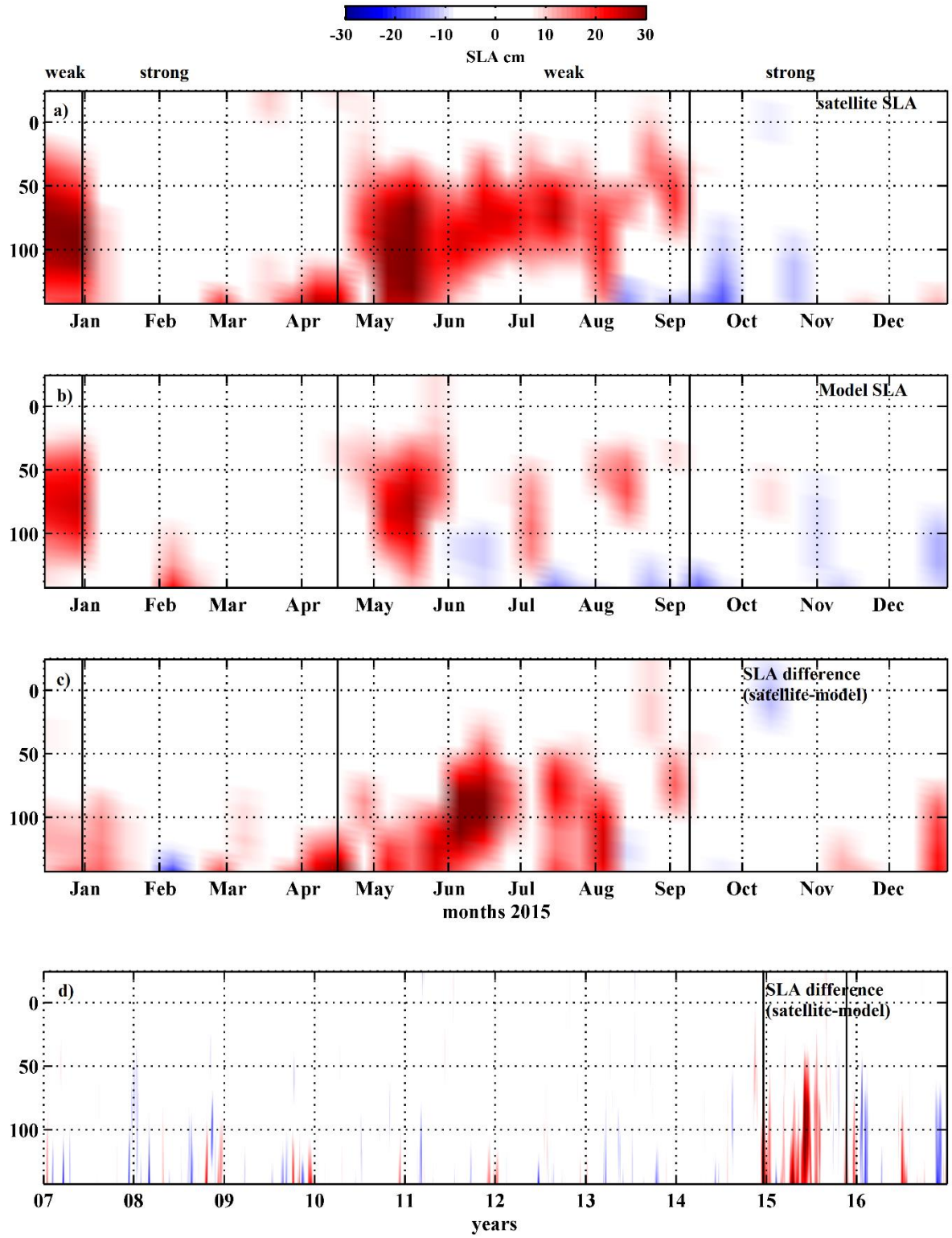
-30 -20 -10 0 10 20 30
SLA cm
weak
strong
weak
strong
a)
satellite SLA
b)
Model SLA
c)
SLA difference
(satellite-model)
0
50
100
Jan Feb Mar Apr May Jun Jul Aug Sep Oct Nov Dec
months 2015
d)
SLA difference
(satellite-model)
07 08 09 10 11 12 13 14 15 16
years

Figure 7

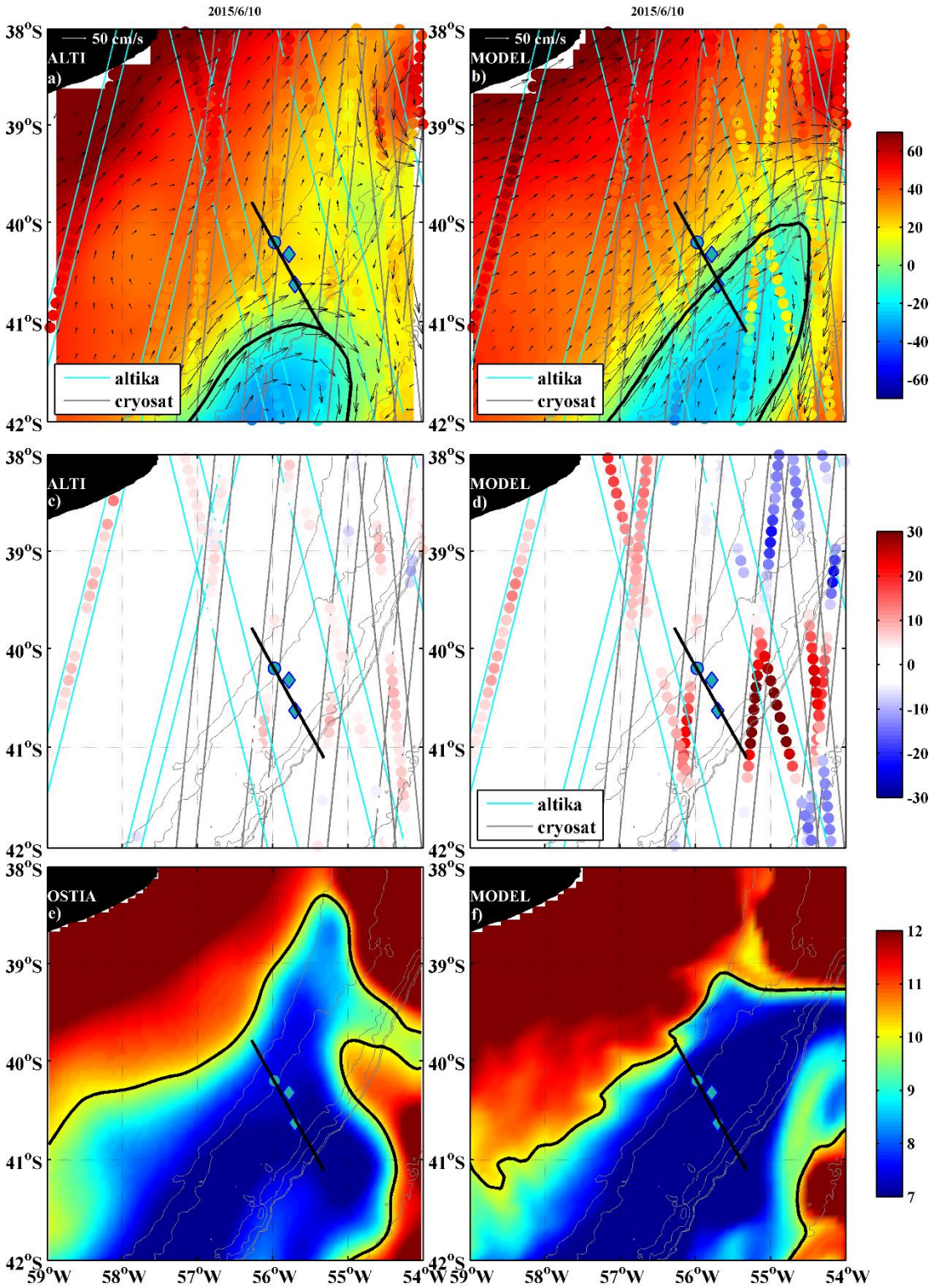
2015/6/10
2015/6/10
50 cm/s
ALTI
a)
50 cm/s
MODEL
b)
altika
cryosat
altika
cryosat
ALTI
c)
MODEL
d)
altika
cryosat
OSTIA
e)
MODEL
f)
38°S
39°S
40°S
41°S
42°S
59°W
58°W
57°W
56°W
55°W
54°W
60
40
20
0
-20
-40
-60
30
20
10
0
-10
-20
-30
12
11
10
9
8
7

Figure 8

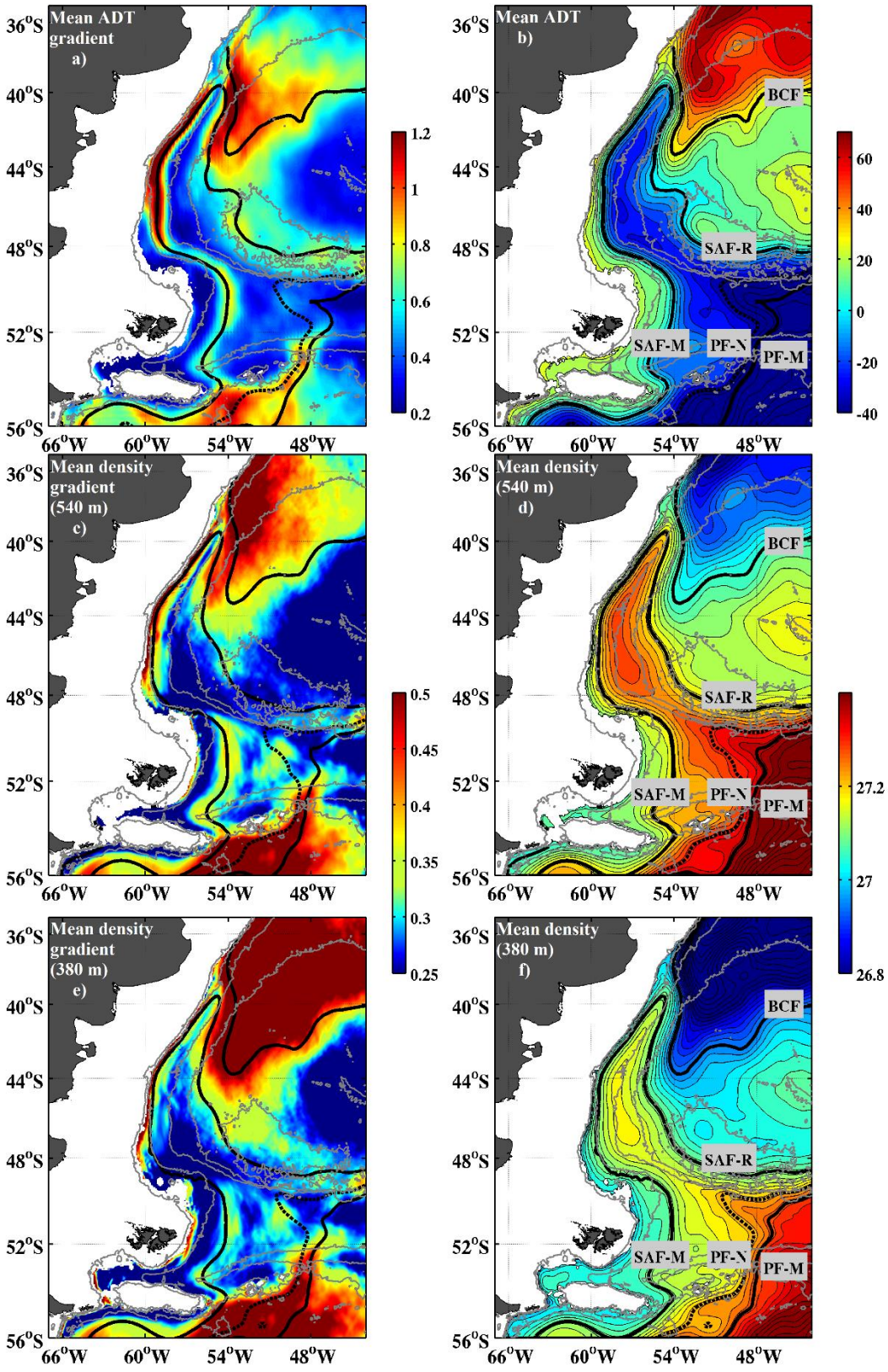
Mean ADT gradient a)
Mean ADT b)
BCF
SAF-R
SAF-M
PF-N
PF-M
Mean density gradient (540 m) c)
Mean density (540 m) d)
Mean density gradient (380 m) e)
Mean density (380 m) f)
36°S
40°S
44°S
48°S
52°S
56°S
66°W
60°W
54°W
48°W
1.2
1
0.8
0.6
0.4
0.2
60
40
20
0
-20
-40
0.5
0.45
0.4
0.35
0.3
0.25
27.2
27
26.8

Figure 9

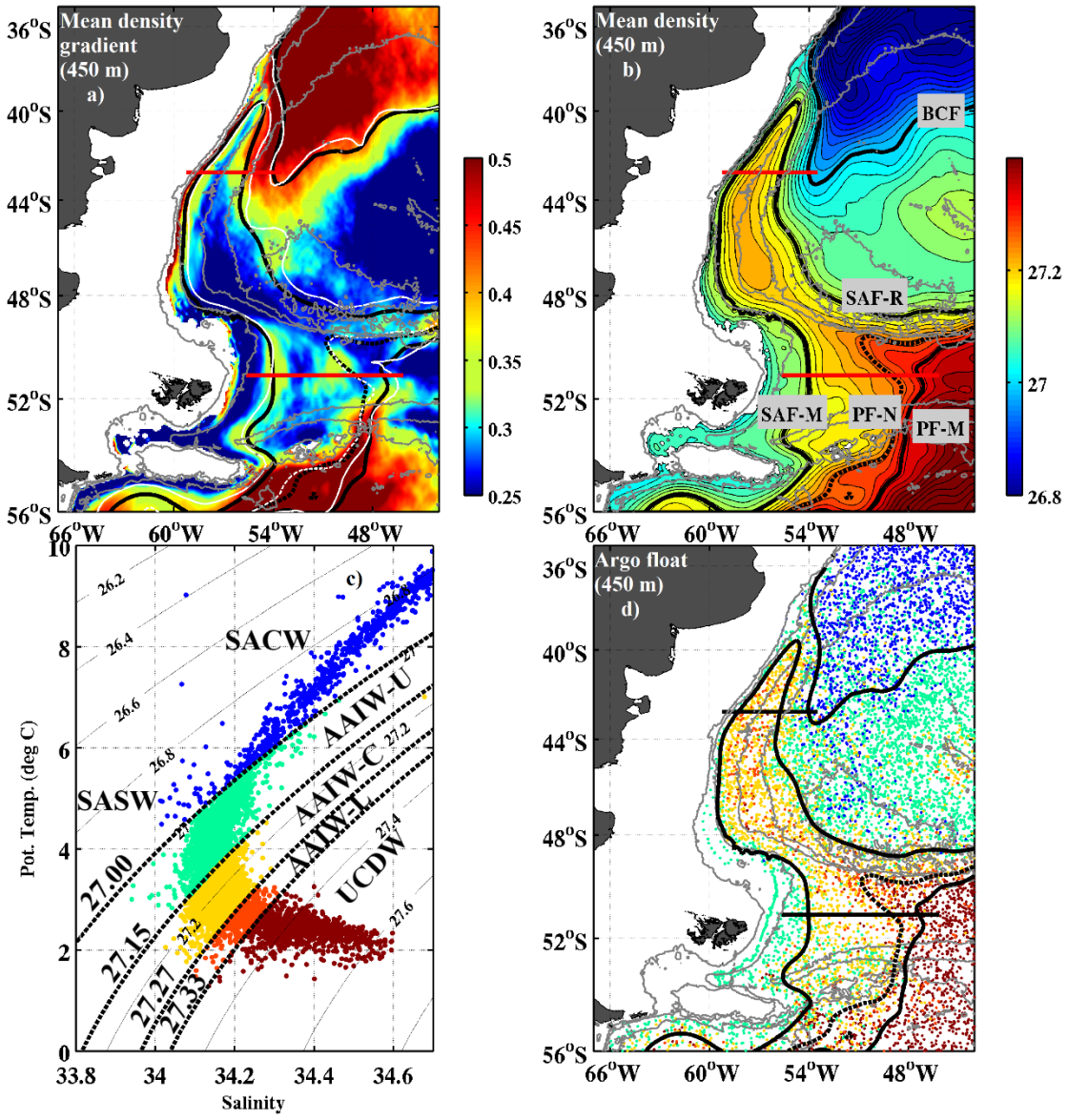
Mean density gradient (450 m)
a)
Mean density (450 m)
b)
BCF
SAF-R
SAF-M
PF-N
PF-M
Argo float (450 m)
d)
c)
SACW
AAIW-U
AAIW-C
AAIW-L
UCDW
SASW
27.00
27.15
27.27
27.33
Pot. Temp. (deg C)
Salinity
36°S
40°S
44°S
48°S
52°S
56°S
66°W
60°W
54°W
48°W

Figure 10

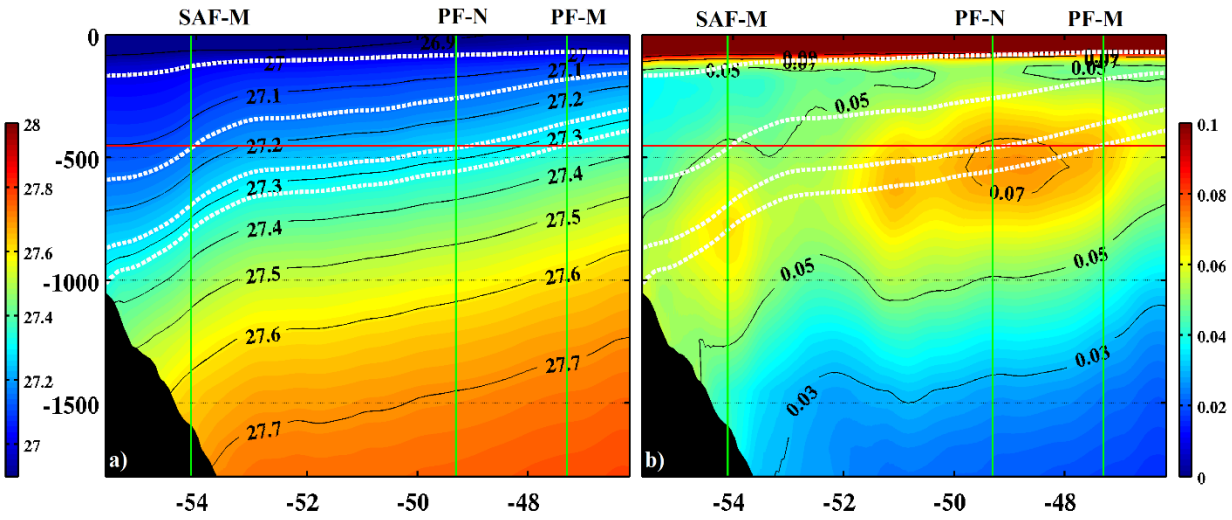
SAF-M
PF-N
PF-M
0
-500
-1000
-1500
28
27.8
27.6
27.4
27.2
27
27.1
27.2
27.3
27.4
27.5
27.6
27.7
a)
-54
-52
-50
-48
0.1
0.08
0.06
0.04
0.02
0
0.05
0.07
0.03
b)

Figure 11

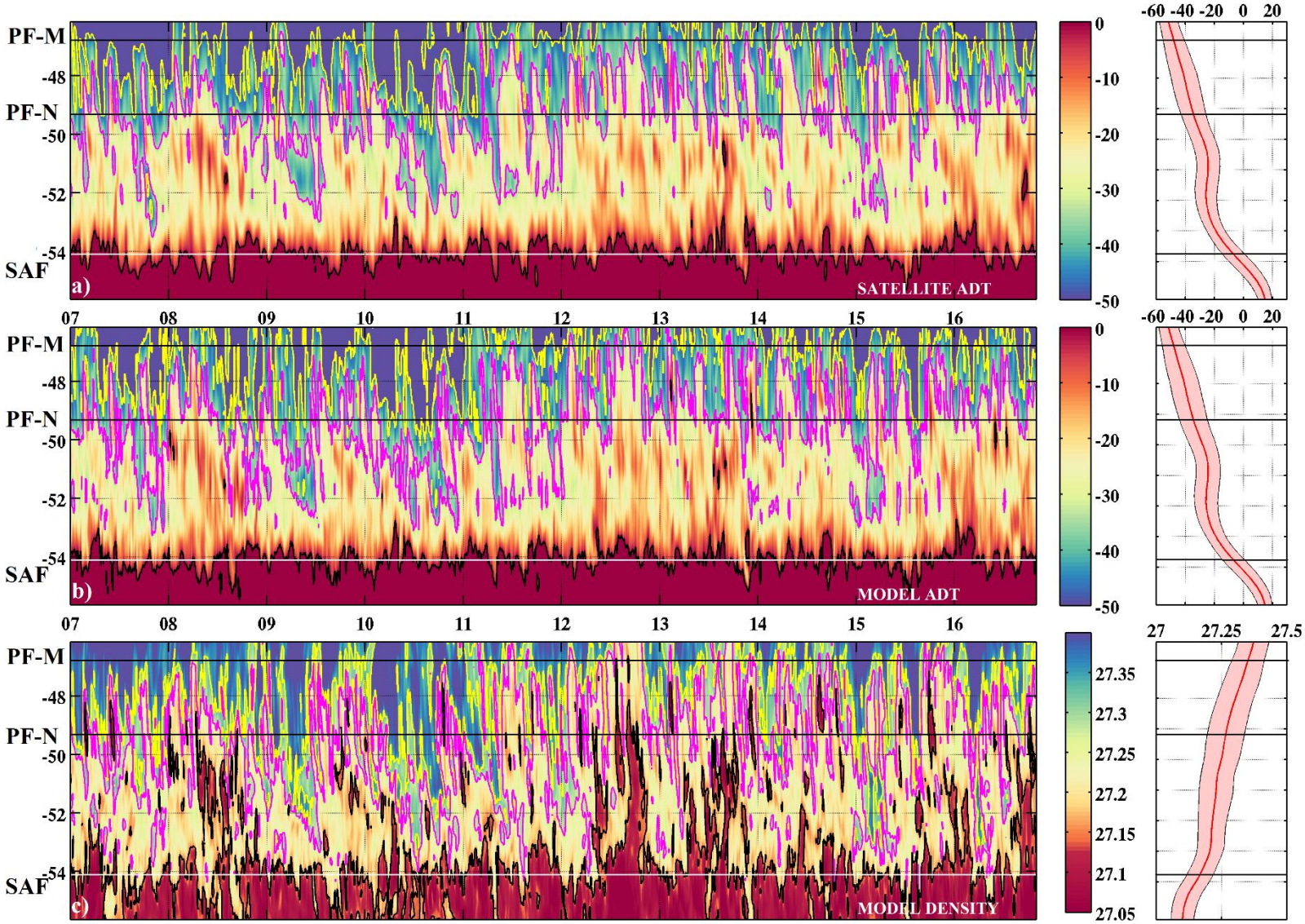
PF-M
PF-N
SAF
-48
-50
-52
-54
a)
SATELLITE ADT
b)
MODEL ADT
c)
MODEL DENSITY
07
08
09
10
11
12
13
14
15
16
0
-10
-20
-30
-40
-50
-60 -40 -20 0 20
27.35
27.3
27.25
27.2
27.15
27.1
27.05
27
27.25
27.5

Figure 12

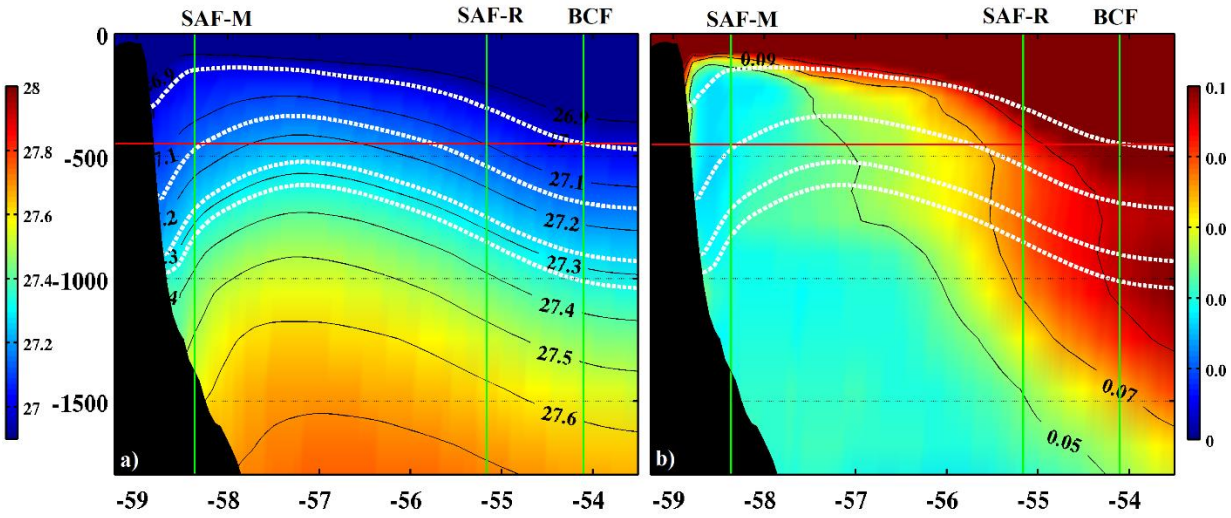
SAF-M
SAF-R
BCF
SAF-M
SAF-R
BCF
0
-500
-1000
-1500
28
27.8
27.6
27.4
27.2
27
26.9
27.1
27.2
27.3
27.4
27.5
27.6
0.09
0.07
0.05
0.1
0.0
0.0
0.0
0.0
0
a)
b)
-59
-58
-57
-56
-55
-54
-59
-58
-57
-56
-55
-54

Figure 13

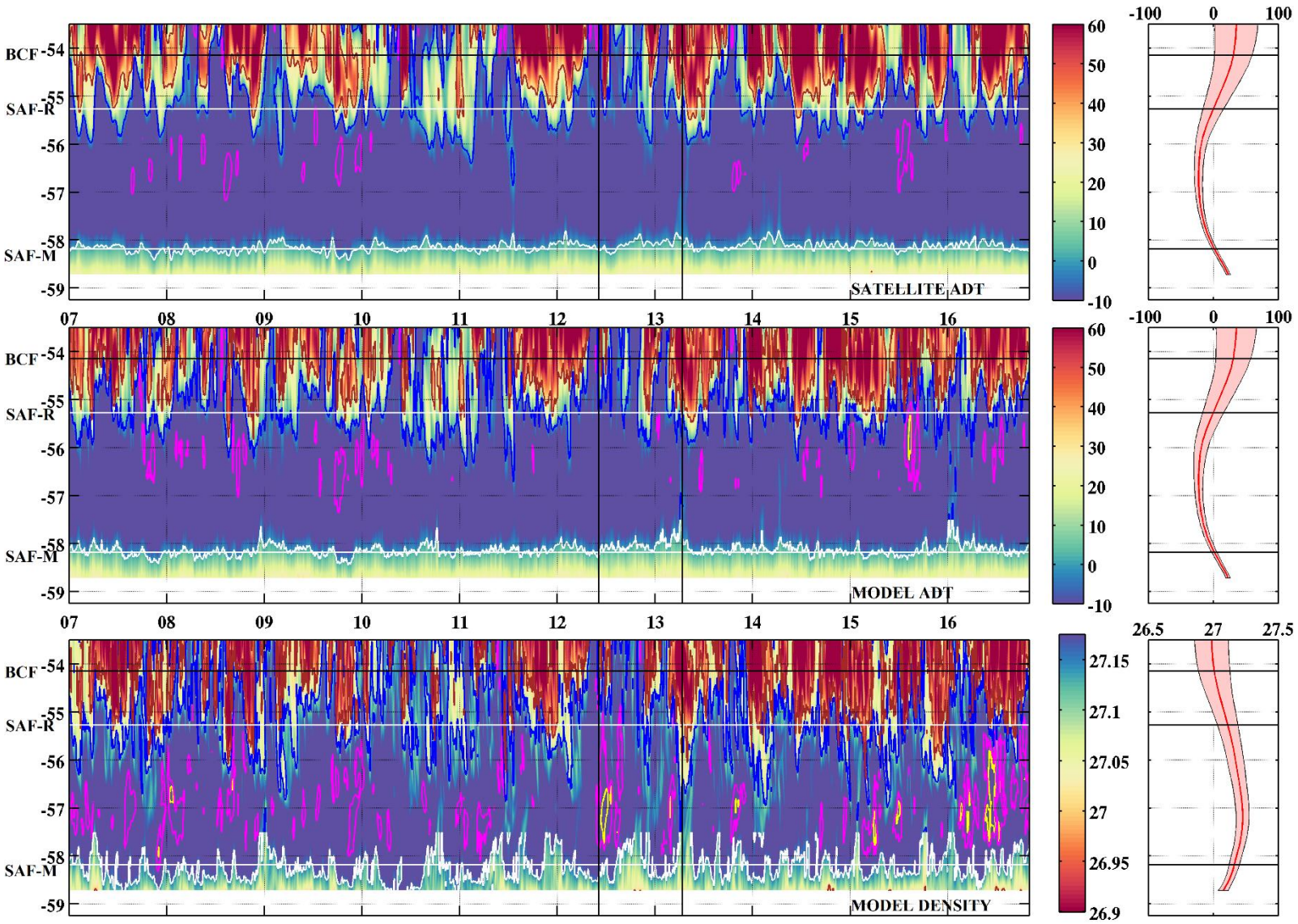
BCF
SAF-R
SAF-M
-54
-55
-56
-57
-58
-59
07
08
09
10
11
12
13
14
15
16
SATELLITE ADT
MODEL ADT
MODEL DENSITY
60
50
40
30
20
10
0
-10
-100
0
100
27.15
27.1
27.05
27
26.95
26.9
26.5
27
27.5

Figure 14

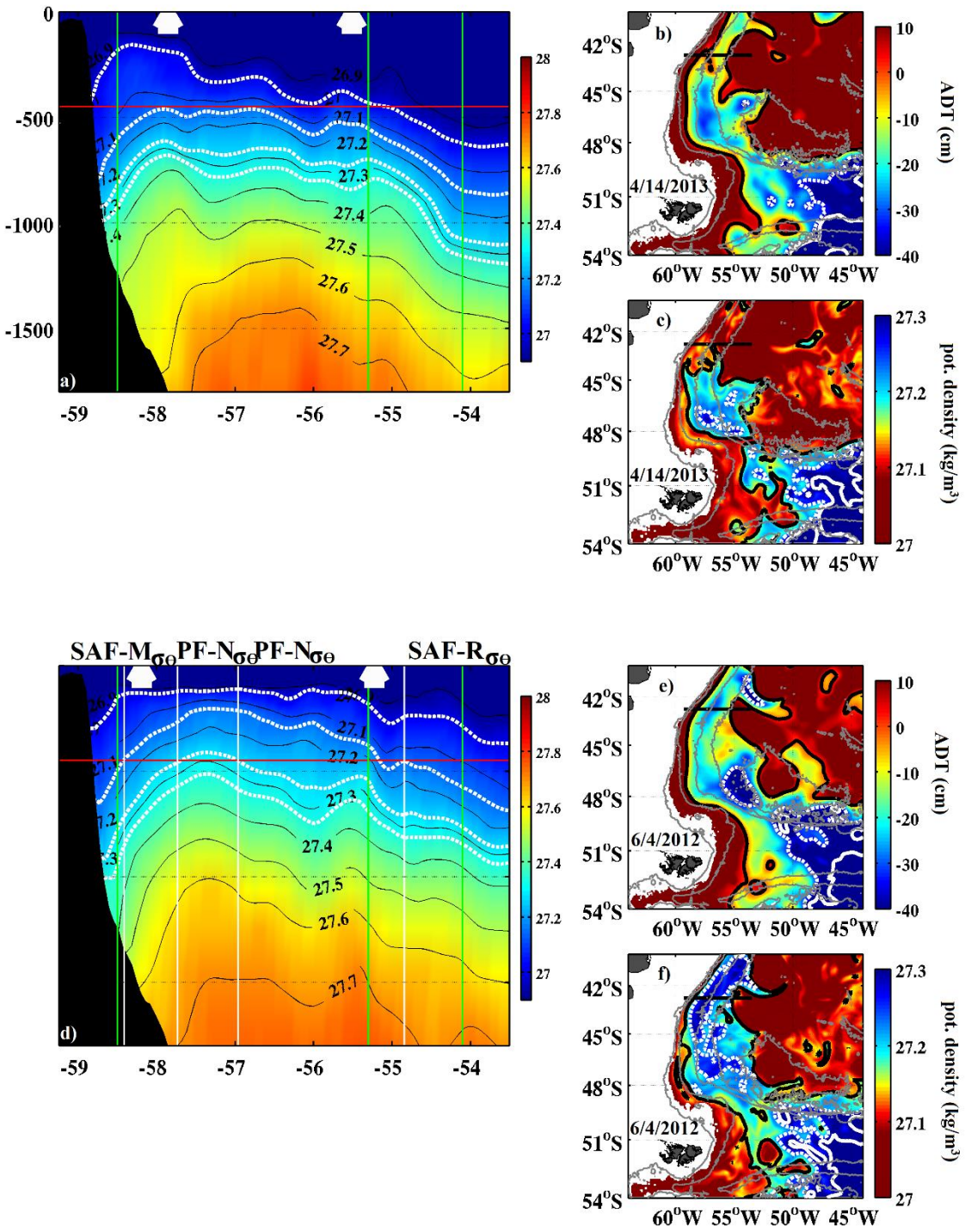
a)
b)
c)
d)
e)
f)
SAF-M$_{\sigma\Theta}$
PF-N$_{\sigma\Theta}$
PF-N$_{\sigma\Theta}$
SAF-R$_{\sigma\Theta}$
4/14/2013
6/4/2012
ADT (cm)
pot. density (kg/m^3)
42°S
45°S
48°S
51°S
54°S
60°W 55°W 50°W 45°W
-59 -58 -57 -56 -55 -54
0
-500
-1000
-1500

Figure 15

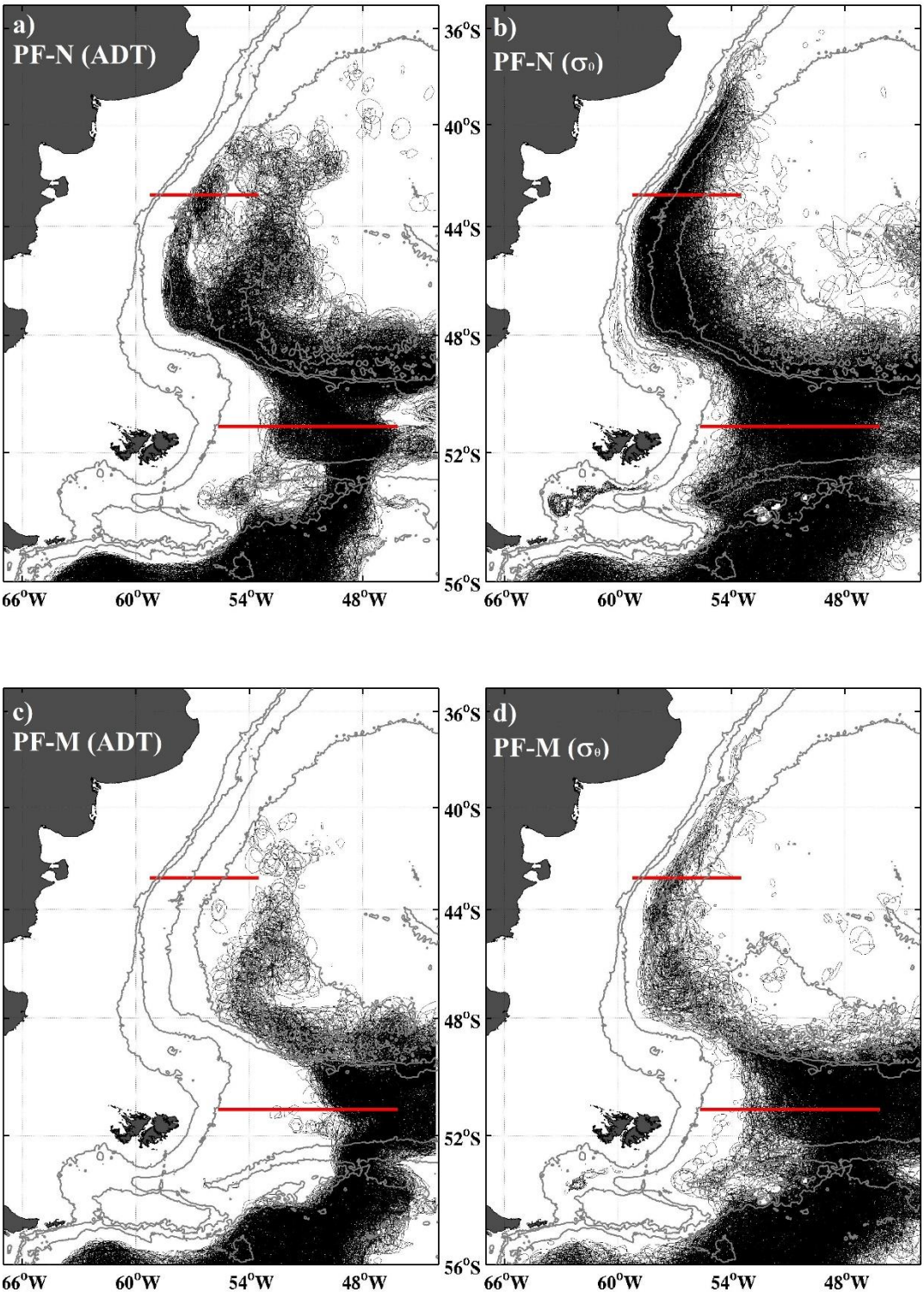
a)
PF-N (ADT)
b)
PF-N (σ₀)
c)
PF-M (ADT)
d)
PF-M (σθ)
36°S
40°S
44°S
48°S
52°S
56°S
66°W
60°W
54°W
48°W

Figure 16

Tables:

Table 1:

	Depth (m)	T in situ μ (σ)	T model μ (σ)	Rmsda T	S in situ μ (σ)	S model μ (σ)	Rmsda S	D in situ μ (σ)	D model μ (σ)	Rmsda D	V // in situ μ (σ)	V// model μ (σ)	Rmsda V //	$V_{\perp}$ in situ μ (σ)	$V_{\perp}$ model μ (σ)	Rmsda $V_{\perp}$
A1	328										33.15 (20.89)	32.08 (19.30)	13.50	-10.11 (8.92)	-6.92 (7.85)	6.64
	544										26.28 (17.67)	26.17 (17.12)	14.15	-8.28 (7.68)	-5.50 (5.83)	7.19
	763										18.55 (12.45)	18.75 (13.50)	14.89	-5.48 (5.27)	-4.17 (4.36)	8.34
	960	3.05 (0.16)	3.25 (0.23)	0.18	34.24 (0.05)	34.23 (0.06)	0.05	27.28 (0.05)	27.21 (0.06)	0.05	12.53 (9.09)	11.65 (11.59)	15.96	-1.61 (2.03)	-1.17 (3.59)	13.19
M1	380	3.99 (0.61)	4.12 (0.43)	0.46							33.35 (22.45)	41.09 (18.69)	17.24	-5.40 (8.92)	-4.21 (9.92)	745
	829	3.25 (0.41)	3.22 (0.31)	0.28	34.23 (0.08)	34.24 (0.07)	0.05	27.26 (0.09)	27.26 (0.08)	0.06	21.22 (15.12)	29.31 (15.06)	11.93	-0.61 (4.85)	-3.69 (6.94)	8.59
	1116	2.85 (0.18)	2.89 (0.37)	0.26	34.35 (0.07)	34.36 (0.09)	0.06	27.39 (0.07)	27.39 (0.09)	0.06	14.10 (16.65)	15.62 (10.73)	8.66	-2.95 (3.64)	-2.19 (3.77)	3.23
M2	524	3.35 (0.57)	3.33 (0.35)	0.45	34.18 (0.04)	34.20 (0.05)	0.03	27.20 (0.09)	27.22 (0.06)	0.06	26.34 (16.13)	38.43 (9.57)	20.13	-3.32 (15.32)	2.74 (12.16)	11.60
	978	2.84 (0.29)	2.66 (0.22)	0.25	34.42 (0.08)	34.47 (0.09)	0.06	27.44 (0.09)	27.50 (0.08)	0.06	19.18 (10.72)	26.64 (10.14)	13.53	0.64 (8.20)	-0.30 (6.88)	6.59
	1275	2.62 (0.18)	2.51 (0.21)	0.11	34.54 (0.08)	34.53 (0.09)	0.07	27.49 (0.08)	27.56 (0.08)	0.06	11.82 (8.62)	21.21 (10.89)	8.96	2.95 (4.99)	-1.18 (4.83)	4.80
	1677	2.36 (0.05)	2.39 (0.23)	0.27	34.60 (0.02)	34.62 (0.07)	0.07	27.59 (0.02)	27.64 (0.05)	0.07	5.94 (3.94)	15.53 (10.18)	10.27	-0.63 (1.43)	-2.35 (4.32)	2.00

Table 2:

Water mass	**Potential density (kg/m^3)**
SASW/SACW	**$27.00<\sigma$**
AAIW-U	**$27.00<\sigma<27.14$**
AAIW-C	**$27.14<\sigma<27.29$**
AAIW-L	**$27.29<\sigma<27.35$**
UCDW	**$27.35<\sigma<27.73$**
CDW	**$27.73<\sigma<27.80$**
LCDW	**$27.73<\sigma<27.83$**

Tables 3

Front	Mean ADT (cm)	Potential density at 380 m (kg/m^3)	Potential density at 450 m (kg/m^3)	Potential density at 540 m (kg/m^3)
BCF	**30**	**26.96**	**27.00**	**27.19**
SAF-M	**0**	**27.11**	**27.15/27.10**	**27.31**
PF-N	**3-34**	**27.23**	**27.27**	**27.37**
PF-M	**-48**	**27.29**	**27.33**	**27.06**

Tables 4 :

location of the time series	R between model ADT and CMEMS gridded produc time series	R between model ADT and potential density time series
Section at 43S		
SAF (-54.1°W,-51.1°S)	**0.8**	**0.7**
PF-N (-49.3°W,-51.1°S)	**0.7**	**0.7**
PF (-46.8°W,-51.1°S)	**0.7**	**0.8**
Section at 51 S		
SAF (-58.3°W,-42.8°S)	**0.6**	**0.6**
SAF-R (-55.3°W,-42.8°S)	**0.6**	**0.7**
BCF (-54.1°W,-42.8°S)	**0.7**	**0.8**